UNIVERSITÀ
DI PAVIA

UNIVERSITY OF PAVIA
FACULTY OF ENGINEERING
DEPARTMENT OF ELECTRICAL, COMPUTER AND BIOMEDICAL ENGINEERING

MASTER'S DEGREE IN ELECTRONIC ENGINEERING

MASTER THESIS

Design of a differential dielectric sensor based on a hybrid coupler on inverted microstrip technology

Progetto di un sensore dielettrico differenziale basato su un accoppiatore ibrido in tecnologia a microstriscia invertita

Candidate: Andrea Minichini

Supervisor: Prof. Lorenzo Silvestri
Co-supervisor: Prof. Maurizio Bozzi
Co-supervisor: Dott. Nicolò Delmonte

A.Y. 2023/2024

Abstract

English

The master thesis is concerned with the design of a sensor for the differential dielectric characterization of liquid materials. The sensor is based on a 'rat-race' hybrid coupler, realized using the inverted microstrip technology, combined with two containers holding different liquid materials. The structure is produced through a hybrid technology, integrating the standard 'printed circuit board' (to build the inverted microstrip) with 3D printing (to realize the containers and the support structure). The dielectric characteristics of a liquid material can be derived by comparing the reflection properties of this liquid with a known calibration material. Different liquid materials are employed to validate the performance of the fabricated device, comparing simulations and measurements.

Italiano

La tesi riguarda la progettazione di un sensore per la caratterizzazione dielettrica differenziale di materiali liquidi. Il sensore è basato su un accoppiatore ibrido di tipo 'rat-race', realizzato utilizzando la tecnologia della microstriscia invertita, combinato con due piccoli serbatoi contenenti differenti liquidi. La struttura è prodotta attraverso una tecnologia ibrida, che integra la tecnica 'printed circuit board' standard (per costruire la microstriscia invertita) con la stampa 3D (per realizzare i serbatoi e la struttura di supporto). Le caratteristiche dielettriche di un materiale liquido possono essere ricavate confrontando le proprietà di riflessione del segnale con quelle di un liquido di calibrazione conosciuto. Per la validazione delle prestazioni del dispositivo fabbricato, sono utilizzati diversi materiali liquidi, andando a confrontare simulazioni e misure.

Index

Introduction

A microwave dielectric sensor is a device able to characterize materials from the point of view of their dielectric properties. It works by exploiting the interactions between the dielectric materials and the electromagnetic fields. In particular, it is possible to determine the complex permittivity of dielectric materials measuring the frequency response of the scattering parameters.

These sensors can have many applications, from bioengineering to radar and remote sensing applications. The purpose is to create small and inexpensive devices, capable to characterize accurately solid, liquid or gaseous materials in real-time. In this sense, these devices fit in the perspective of growing Internet of Things (IoT) applications. With the development of IoT, the demand for wireless sensors is constantly increasing.

Going through the fabrication techniques, nowadays an interesting field of research is 3D printing. This manufacturing method is characterized by a great design flexibility, at a relatively low cost. 3D printing can be employed to realize a sensor, entirely or in combination with other technologies.

Many topologies of dielectric sensors have been investigated, on the basis of working principle, analysed materials and methods of realization.

In this thesis work, the purpose is the design and the realization of a sensor for a differential dielectric characterization of liquid materials. The chosen topology is a rat-race hybrid coupler - realized through an inverted microstrip - combined with two containers holding different liquid materials. The dielectric characteristics of a liquid under test (LUT) can be derived from the comparison of the reflection properties of the LUT with a calibration material, whose properties are known. The fabrication of the sensor involves a hybrid technology, which combines a standard printed circuit board (used to build the inverted microstrip) with 3D printing (used to manufacture the containers and the support structure).

More in detail, the Chapter 1 contains a theoretical description of the electromagnetic properties of dielectric materials with an overview of the techniques used to characterize these materials.

In the Chapter 2, the discussion concerns the design and the analysis of the sensor. In the initial part, there are explained the technology and the topology chosen for the sensor, thus its working principle. Then, there are shown the design stages of the device, making an analytical study of the component. The results are obtained through simulations, employing the commercial simulation tools Cadence AWR and Ansys HFSS.

Finally, to validate the experimental results, the Chapter 3 illustrates the fabrication and the measurements of a prototype of the sensor, comparing the results with simulations.

Chapter 1

Dielectrics and sensors

1.1 Electromagnetic properties of materials

Dielectric sensors base their functioning on the interactions between a dielectric material and the electromagnetic fields [1]. These phenomena can be described using Maxwell's equations:

$$\nabla \cdot \boldsymbol{D} = \rho$$

$$\nabla \cdot \boldsymbol{B} = 0$$

$$\nabla \times \boldsymbol{H} = \frac{\partial \boldsymbol{D}}{\partial t} + \boldsymbol{J}$$

$$\nabla \times \boldsymbol{E} = -\frac{\partial \boldsymbol{B}}{\partial t}$$

with the following constitutive equations:

$$\boldsymbol{D} = \varepsilon \boldsymbol{E} = (\varepsilon' - j\varepsilon'')\boldsymbol{E}$$

$$\boldsymbol{B} = \mu \boldsymbol{H} = (\mu' - j\mu'')\boldsymbol{H}$$

$$\boldsymbol{J} = \sigma \boldsymbol{E}$$

where **H** represents the magnetic field; **E** the electric field; **B** the magnetic induction; **D** the electric displacement vector; **J** the current density vector; ρ the charge density; $\varepsilon = \varepsilon' - j\varepsilon''$, the electric permittivity of the material; $\mu = \mu' - j\mu''$, the magnetic permeability of the material; and σ the conductivity of the material.

The response of a material to electromagnetic fields is determined fundamentally by three constitutive parameters: the permittivity ε, the permeability μ and the

conductivity σ. It is important to notice that, in general, these parameters are frequency dependent: for example, they can determine how much the electromagnetic field penetrates inside the substance at a given frequency. Among this kind of parameters, we will focus on the permittivity ε, which is in general a complex value.

It is possible to distinguish between low-conductivity materials and high-conductivity materials. We will focus on the first type.

Electromagnetic waves can propagate in a low-conductivity material, and both its surface and inner parts respond to them. The electromagnetic properties of these substances are described, in addition to the constitutive parameters, also by the propagation parameters.

Now, we consider a circuit with lumped elements, as in Figure 1.1.

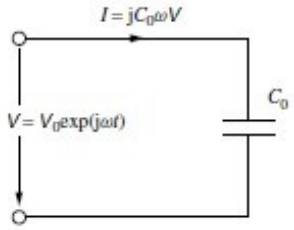

Figure 1.1 – Current in a circuit with capacitor.

The vacuum capacitor with capacitance C_0 is connected to an AC voltage source $V = V_0 e^{j\omega t}$. The charge storage in the capacitor is $Q = C_0 V$, and the current I flowing in the circuit is $I = \frac{dQ}{dt} = \frac{d}{dt}(C_0 V_0 e^{j\omega t}) = j\omega C_0 V$.

Inserting a dielectric material inside the capacitor, the total current is the sum of two contributions, the charging current (I_c) and the loss current (I_l), so:

$$I = I_c + I_l = j\omega CV + GV = (j\omega C + G)V$$

where C is the capacitance of the capacitor loaded with the dielectric and G is the conductance of the dielectric (as shown in the equivalent circuit in Figure 1.2a).

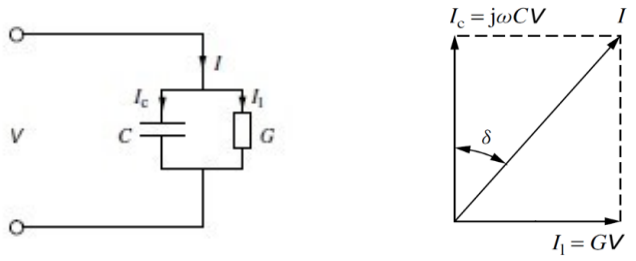

a) *b)*

Figure 1.2 - Charging current and loss current: (*a*) equivalent circuit; (*b*) complex plane.

It can be noted that the total current *I* is a complex quantity: the loss current, I_l, is the real part, while the modulus of the charging current, I_c, is the imaginary part. Thus, in a complex plane (Fig. 1.2b), I_l will be on the real axis and I_c on the imaginary one and, in this way, it can be defined *loss angle* δ the angle between I_c and *I*.

The effect of the insertion of a dielectric material can be described also through the complex permittivity $\varepsilon = \varepsilon' - j\varepsilon''$. In fact, the introduction of a dielectric into a capacitor changes the capacitance C in this way:

$$C = \frac{\varepsilon C_0}{\varepsilon_0} = (\varepsilon' - j\varepsilon'')\frac{C_0}{\varepsilon_0}$$

Therefore, the charging current is:

$$I_c = j\omega CV = j\omega(\varepsilon' - j\varepsilon'')\frac{C_0}{\varepsilon_0}V = (j\omega\varepsilon' + \omega\varepsilon'')\frac{C_0}{\varepsilon_0}V$$

The quantity $\omega\varepsilon''$ is equivalent to a dielectric conductivity (σ): this quantity sums all the dissipative effects of the material.

To describe the energy dissipation of a dielectric material, it can be defined a parameter, the dielectric loss tangent, $\tan\delta_e = \varepsilon''/\varepsilon'$, where δ_e is the dielectric loss angle.

Other quantities used in microwave electronics are the relative permittivity ε_r and the quality factor Q (especially the dielectric quality factor Q_e), defined by:

$$\varepsilon_r = \frac{\varepsilon}{\varepsilon_0} = \frac{\varepsilon' - j\varepsilon''}{\varepsilon_0} = \varepsilon_r{}' - j\varepsilon_r{}''$$

$$Q_e = \frac{\varepsilon_r{}'}{\varepsilon_r{}''} = \frac{1}{\tan\delta_e}$$

where $\varepsilon_0 = 8.854\times10^{-12}$ F/m is the vacuum permittivity.

The propagation parameters describe the propagation of electromagnetic waves in a medium: they are the characteristic wave impedance, or intrinsic impedance of the medium, η, and the wave velocity in the medium, v.

η is defined as the ratio between the total electric field and the total magnetic field; it is also possible to use permittivity and permeability to define η and v, so:

$$\eta = \sqrt{\frac{\mu}{\varepsilon}}$$

$$v = \frac{1}{\sqrt{\mu\varepsilon}}$$

In free space, since $\varepsilon = \varepsilon_0$ and $\mu = \mu_0 = 4\pi \times 10^{-7}$ H/m, then $\eta = \eta_0 = 377\ \Omega$ and $v = c = 3 \times 10^8$ m/s.

Moreover, to characterize the propagation of an electromagnetic wave in a medium, it is used the propagation coefficient $\gamma = \alpha + j\beta = j\omega\sqrt{\mu\varepsilon}$, in which α is the attenuation constant, $\beta = 2\pi/\lambda$ is the phase constant, λ is the wavelength in the medium and ω is the angular frequency.

1.2 Techniques for material characterization

The microwave methods for material characterization can be non-resonant or resonant [1].

The non-resonant methods are commonly used for a general knowledge of electromagnetic properties over a frequency range, while the resonant methods are

often used for an accurate knowledge of dielectric properties at a single frequency. Both can be used in combination.

In non-resonant methods, it is possible to determine the properties of materials through the impedance and the wave velocity: when an electromagnetic wave passes from one medium to another, both these parameters change. A partial reflection of the wave occurs at the interface between the two media: the reflection measurement at the interface and the transmission measurement through it can deliver information about permittivity and permeability relationship between the two materials. Generally, transmission lines are used to detect the waves, such as coaxial cables and waveguides.

The main non-resonant methods are reflection and transmission/reflection.

In the reflection methods, electromagnetic waves are directed towards a sample under test: the characteristics of the material are detected from the reflection coefficient at a defined reference plane. Generally, a reflection method measures a single parameter, either permittivity or permeability. There exist two kinds of reflection approaches to characterize low-conductivity materials: the open-reflection and the shorted-reflection methods. Coaxial lines, which can cover broad frequency bands, are usually employed for these techniques.

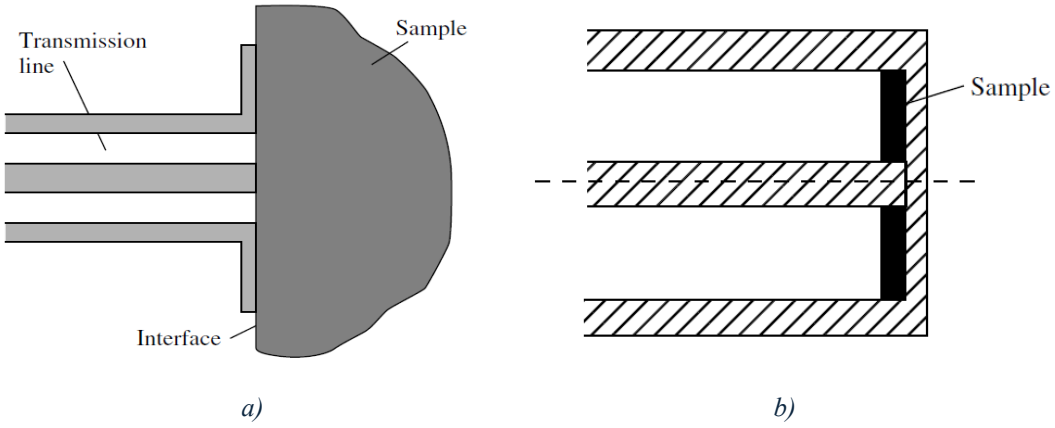

Figure 1.3 – Reflection methods: (*a*) Coaxial dielectric probe; (*b*) Coaxial short-circuit reflection.

The open-reflection technique is characterized by the so-called *coaxial dielectric probe*, in which a nonmagnetic material is positioned in contact with a coaxial line, as in Figure 1.3a. Here, the assumption is that the probe does not sense the interactions between the electromagnetic field and the non-contacting boundaries of the sample. Hence, the sample should be much larger than the diameter of the aperture of the open-ended coaxial line, and the material should have enough loss.

In the short-reflection technique (Figure 1.3b), the substance under test is typically electrically short: this method is normally employed to measure magnetic permeability, since the measurements are not sensitive to the permittivity of the sample.

It is possible to represent the reflection method with an equivalent circuit (shown in Figure 1.4), in which the impedance Z of the coaxial aperture depends on the relative permittivity ε_r of the sample under test. The dielectric sample positioned at the end of the coaxial probe is comparable to introduce the sample in an equivalent capacitor, hence the impedance in the circuit can be replaced by a capacitance.

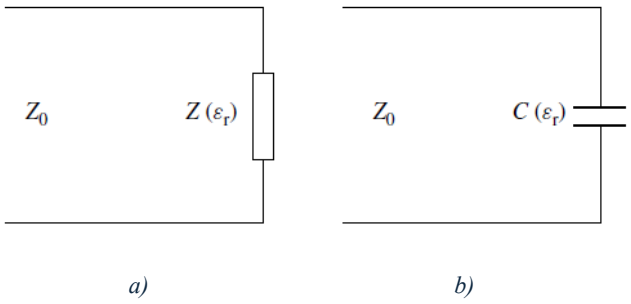

Figure 1.4 - Equivalent circuits for reflection methods with impedance (*a*) and capacitance (*b*).

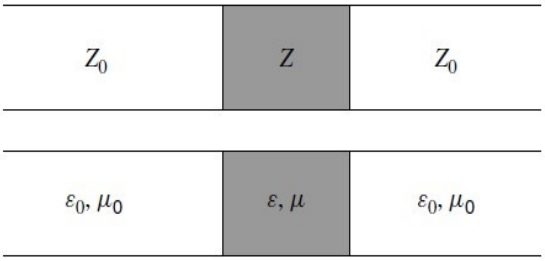

Figure 1.5 – Coaxial transmission/reflection method.

In the transmission/reflection methods (Figure 1.5), the material under test is introduced inside a piece of transmission line, such that the properties can be determined by the reflection from the material and the transmission through it. This technique is commonly utilized to measure permittivity and permeability of low-conductivity materials. Referring to the Figure 1.5, it is possible to notice that the characteristic impedance of the part of transmission line loaded with the sample is different from the piece of line without the sample. This difference results in particular transmission and reflection features at the interface: thanks to the resulting reflection and transmission coefficients, permittivity and permeability are obtained.

Passing to the resonant methods, they typically have better accuracies and sensitivities than non-resonant ones and are suitable for low-loss samples. They include the resonator and the resonant-perturbation methods.

In the first technique, also named dielectric resonator method, the resonant frequency and the quality factor of a dielectric resonator are determined by its permittivity and permeability. This approach can be used to get the permittivity of dielectric materials, usually by placing a sample between two conducting plates, such as in Figure 1.6a.

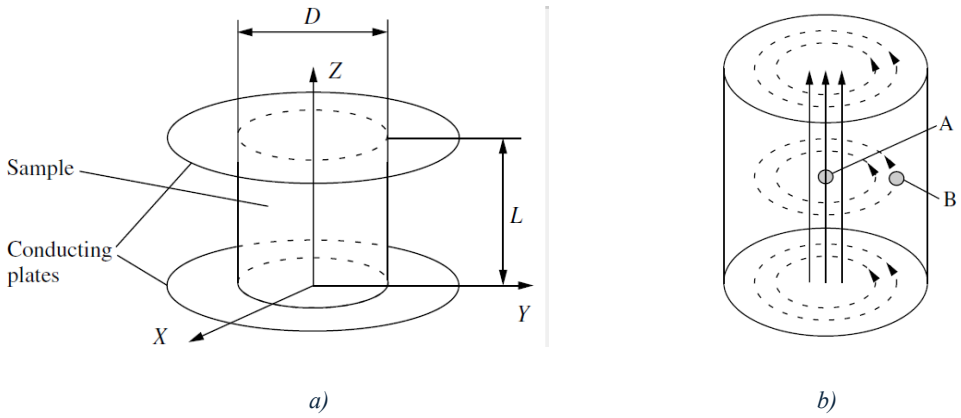

Figure 1.6 – Resonator methods: (*a*) Dielectric resonator; (*b*) Resonant-perturbation.

In the second approach (shown in Figure 1.6b), if a sample is introduced into a resonator, the resonant frequency and the quality factor of the resonator will be changed: from these variations, the properties of the material can be determined. There are different kinds of resonant perturbations, for example cavity shape and wall-loss perturbation. The first one helps to adjust the resonant frequency of a cavity. In the second one, part of the cavity wall is replaced by the examined sample, thus modifying resonant frequency and quality factor.

1.3 Examples of dielectric sensors

In recent years, many studies have been made about the design and the realization of dielectric sensors. These devices can have various applications, for example in bioengineering, radar applications or remote sensing.

An example is a sensor composed of a two-ring planar resonator [2]: through a dropping-based method, the resonant frequency and the quality factor are translated, and the resulting shift is related to the complex permittivity of the liquid. The change in the resonant frequency is exploited also in the solution constituted by an electromagnetic band gap and a suspended microstrip line [3], and in a sensor in which a liquid flows in a pipe inside a resonant cavity, that is based on a substrate integrated waveguide (SIW) [4].

A microfluidic channel on the top of a microwave planar resonator [5] can be filled with a liquid: the interaction between electric field and the fluid leads to a predictable relationship between resonant frequency and complex permittivity of the substance.

Another way to characterize liquids is through a section of an inverted microstrip line with a quarter wavelength open ended stub, in which the liquid under test flows in a channel [6]: the dielectric characteristics are taken from the variation of the frequency response of the structure.

A transmission line loaded with a composite resonator [7] produces a transmission zero and a transmission pole, whose frequencies are modified by the low-loss and lossy dielectric samples, that can be solids or liquids. Solid and liquid materials are also detected by a sensor composed of a branch line coupler [8], where a branch is used for reference and the other one for testing: loading a sample, the electrical length and the characteristic impedance are modified, affecting the isolation level: measuring it, the material is identified.

An open-ended broadside-coupled-line section with a liquid channel between the strips [9] can be used for liquid chemical monitoring through a differential excitation of the sensor: the electric field is located within the channel, so there is a high sensitivity on the measured electrical properties of the sample.

It is also possible to exploit two resonance frequencies for a differential reading, that can permit a highly accurate analysis, for example through a microstrip transmission line loaded with a complementary split ring resonator (CSRR) [10] or through the perturbation of the coupling between two rectangular cavities [11].

As an alternative to methods based on the determination of the resonance frequency shift, it can be employed a SIW cavity resonator with a small pipe [12]: in this case, there is not a frequency sweep, but an instantaneous liquid characterization.

Finally, it can be considered an example of a rotation sensor [13], where the angular displacement is intended in terms of the change in resonant frequency. This sensor is based on a microstrip technology where a rotor comprised of a CSRR rotates; loading the rotor with a dielectric, a change in operating frequencies and bandwidths will occur.

Chapter 2

Design and analysis of the sensor

The design of the sensor is based on a rat-race coupler, built using an inverted microstrip.

2.1 Inverted Microstrip Technology

Microstrip lines are essential elements in microwave integrated circuits [14][15]. They are planar transmission lines that can be easily miniaturized and integrated with both passive and active microwave devices. They can be fabricated with photolithographic processes, with lower costs with respect to waveguides or coaxial lines.

Basically, a microstrip line is made of two parallel conductor lines, of which at least one is a flat strip of small thickness. To guarantee mechanical stability, the strip is placed on a dielectric substrate, generally supported by a metal ground plane. The most important parameters for characterizing the line are the width of the strip W, the thickness of the substrate d and the relative dielectric constant of the substrate ε_r.

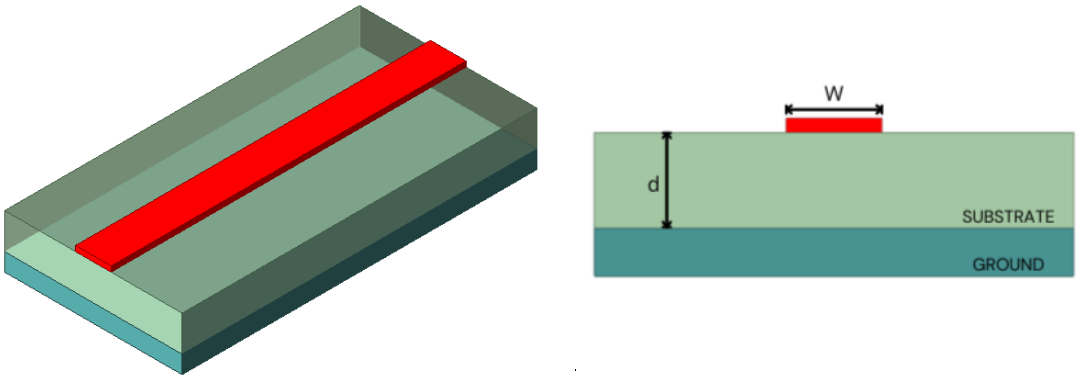

a) *b)*

Figure 2.1 – Standard microstrip line: (*a*) structure; (*b*) section.

The propagating mode would be TEM (transverse electromagnetic) in case the dielectric substrate is not present ($\varepsilon_r = 1$). Nevertheless, the presence of the dielectric, which has not a homogeneous distribution around the strip, prevents the pure TEM mode propagation. This fact is due to the different wave velocities in the air ($v = c$) and in the substrate ($v = c/\sqrt{\varepsilon_r}$), so the phase-matching at the dielectric-air interface does not occur anymore. The result is a hybrid coupling of a TE (transverse electric) and a TM (transverse magnetic) mode. But, since the substrate usually is much thinner than the wavelength ($d \ll \lambda$), it is possible to approximate the propagation mode as a quasi-TEM (Figure 2.2).

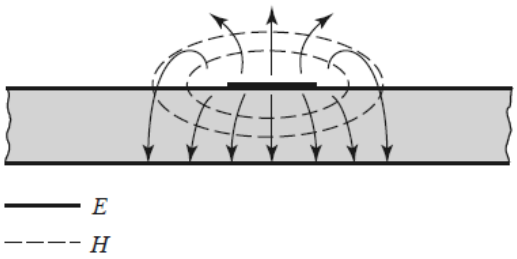

Figure 2.2 – Distribution of fields in a microstrip section.

Some parameters are used to describe the microstrip line, such as impedance Z, wavelength λ, attenuation α and effective dielectric constant ε_{eff}: $Z = \frac{Z_0}{\sqrt{\varepsilon_{eff}}}$; $\lambda = \frac{\lambda_0}{\sqrt{\varepsilon_{eff}}}$; $\alpha = \alpha_0\sqrt{\varepsilon_{eff}}$, where Z_0, λ_0, α_0 are respectively the characteristic impedance, the wavelength and the attenuation per unit length of a line in air. The attenuation is due to the losses from the conductor and the dielectric: typically, in microstrip lines, conductor losses are more significant than dielectric ones. The value of ε_{eff} depends on the fact that some of the field lines are in the substrate and some in the air (Figure 2.2), so $1 \leq \varepsilon_{eff} \leq \varepsilon_r$.

An important fact to consider is that the parameters of a transmission line are frequency dependent. Variations of the parameters can be significant, so in many cases a value of a parameter is valid only for a specific frequency. For example, a frequency variation of the effective dielectric constant produces a phase delay, which grows if the line section is longer.

The configuration in Figure 2.1 can be modified in different ways: among them, we are interested in the inverted microstrip line, in which the substrate is placed above the strip and an air gap takes place between the strip and the ground plane (Figure 2.3). In this case, the presence of the air gap causes the reduction of the effective dielectric constant: in fact, the value of the effective dielectric constant follows the relationship $1 \leq \varepsilon_{eff} \leq \frac{1+\varepsilon_r}{2}$, whereas in the standard line this is $\frac{1+\varepsilon_r}{2} \leq \varepsilon_{eff} \leq \varepsilon_r$. A lower ε_{eff} means that the effective dielectric loss tangent is lower, making possible the realization of larger circuits, with less mechanical issues, and so lower production costs.

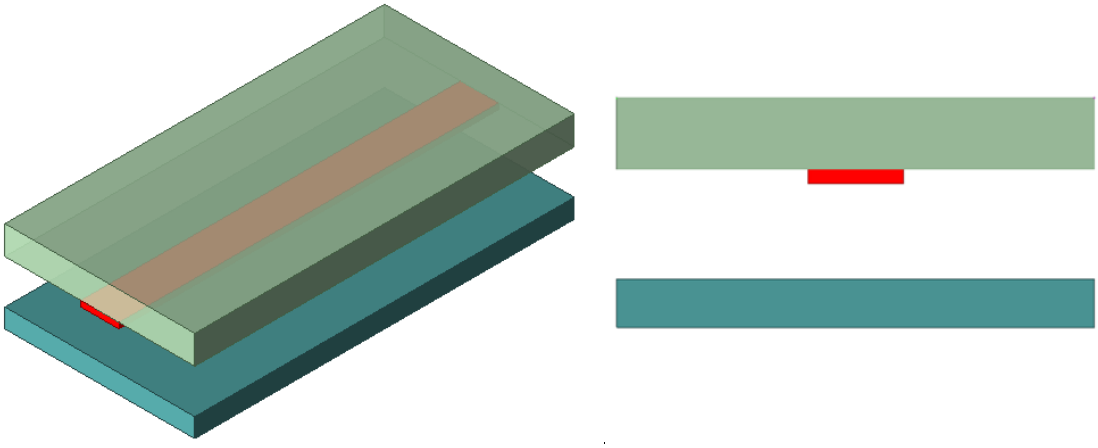

c) *b)*

Figure 2.3 – Inverted microstrip line: (*a*) structure; (*b*) section.

2.2 Power dividers and directional couplers

Power dividers and directional couplers are passive microwave components, in which an input signal is divided in two or more output signals of smaller power, or two or more input signals are combined at the output [15]. They can have three, four, or more ports. According to the configuration, the division ratio of the output signals can be equal or not and output signals can be in-phase or, in the case of hybrid junctions, can have a phase shift of 90° or 180°.

We are interested in the four-port configuration, in which the scattering matrix of a reciprocal network (which has a symmetrical matrix) matched at all ports (so $S_{ii} = 0$) is:

$$[S] = \begin{bmatrix} 0 & S_{12} & S_{13} & S_{14} \\ S_{12} & 0 & S_{23} & S_{24} \\ S_{13} & S_{23} & 0 & S_{34} \\ S_{14} & S_{24} & S_{34} & 0 \end{bmatrix}$$

For a lossless network, results that $S_{14} = S_{23} = 0$, since the matrix is unitary; moreover, $|S_{13}| = |S_{24}|$ and $|S_{12}| = |S_{34}|$. Choosing the phase reference on three out of four ports, we can set $S_{12} = S_{34} = \alpha$, $S_{13} = \beta e^{j\theta}$, and $S_{24} = \beta e^{j\varphi}$, whereas α and β are real, and θ and φ are phase constants to be chosen. Considering that $\alpha^2 + \beta^2 = 1$ and $\theta + \varphi = \pi \pm 2n\pi$, usually there are made two choices for the phase constants (if $n = 0$): the symmetric coupler, where $\theta = \varphi = \pi/2$ and the antisymmetric coupler, where $\theta = 0$ and $\varphi = \pi$.

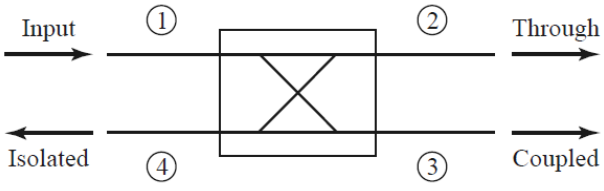

Figure 2.4 – Scheme of a directional coupler.

Referring to the Figure 2.4, in a directional coupler, the signal entering in port 1 (input port) is coupled to port 3 (coupled port), with a specific coupling factor; the remaining part of the power is carried to port 2 (through port) and, ideally, no power is delivered to port 4 (isolated port).

Finally, hybrid couplers are special types of directional couplers, in which the power is equally split between ports 2 and 3: the coupling factor is 3 dB, so $\alpha = \beta = \frac{1}{\sqrt{2}}$. There exist two kinds of hybrids: the quadrature hybrid, which is an example of symmetric coupler (90° phase difference between ports 2 and 3 if power enters at port 1); the magic-T hybrid and the rat-race hybrid, that are examples of antisymmetric couplers (180° phase difference between ports 2 and 3 if power enters at port 4).

2.3 Rat-race couplers

The rat-race (or ring-hybrid) coupler is a type of 180° hybrid junction, which is a four-port network with a 180° phase shift between the two output ports [15].

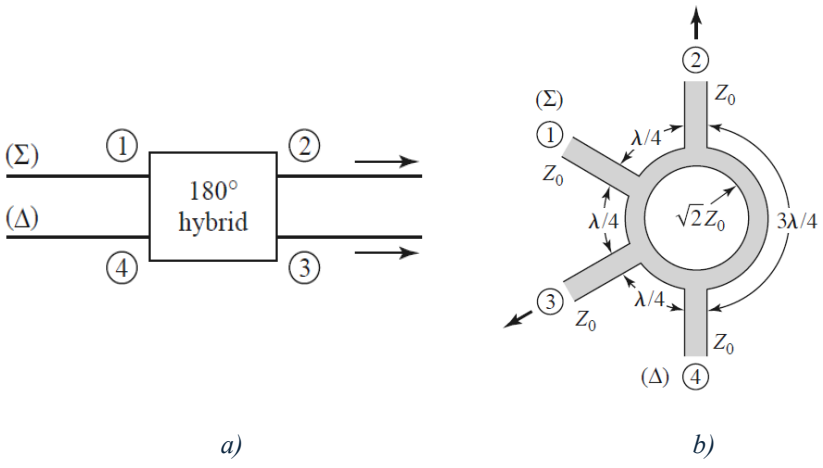

a) *b)*

Figure 2.5 - Schemes of: (*a*) a generic 180° hybrid junction; (*b*) a rat-race.

If an incoming signal is in port 1, it will be equally divided in two in-phase components at ports 2 and 3, and port 4 will be isolated. Instead, if the input signal

is in port 4, it will be equally divided in two components with a 180° phase difference at ports 2 and 3, and port 1 will be isolated. In addition to be used as a power divider, this component can be employed also as a combiner: in this case, the input signals are at ports 2 and 3, and at port 1 there will be the sum of the inputs, while at port 4 the difference. Thus, the port 1 and 4 are called, respectively, sum and difference ports.

The scattering matrix for an ideal 3-dB 180° hybrid is:

$$[S] = -\frac{j}{\sqrt{2}}\begin{bmatrix} 0 & 1 & 1 & 0 \\ 1 & 0 & 0 & -1 \\ 1 & 0 & 0 & 1 \\ 0 & -1 & 1 & 0 \end{bmatrix}$$

The rat-race (Figure 2.5b) is usually realized in planar forms (microstrip or stripline), and less frequently using waveguides. Physical dimensions are strictly related to the wavelength: in fact, taking the Figure 2.5b, the circumference is 1.5λ and the distances between ports 1 and 2, 1 and 3, 3 and 4 is λ/4 (corresponding to an electrical length of 90° for each section), while the distance between ports 2 and 4 is 3λ/4 (that corresponds to an electrical length of 270°). The impedance is Z_0 in correspondence of the port branches, and $\sqrt{2}Z_0$ in the ring.

2.4 The working principle of the sensor

The initial part of the sensor design is made employing the Cadence AWR Software, in order to understand the operative principle of the device. In our case, the signal enters in port 1, then the electrical length between ports 1 and 2 is 270°, while it is 90° between each of the remaining ones. Hence, the phase difference between the output ports 2 and 4 is 180° and port 3 is isolated.

The working principle of the sensor can be explained through linear transmission lines, as shown in Figure 2.6. At each output port (2 and 4), there is an opened line section: the electrical length of one of the two is fixed, and the other one varies. Therefore, the scattering parameter S_{31} varies depending on the difference of the

two electrical lengths. If the difference is zero, S_{31} will be zero and the port 3 will remain isolated, otherwise not.

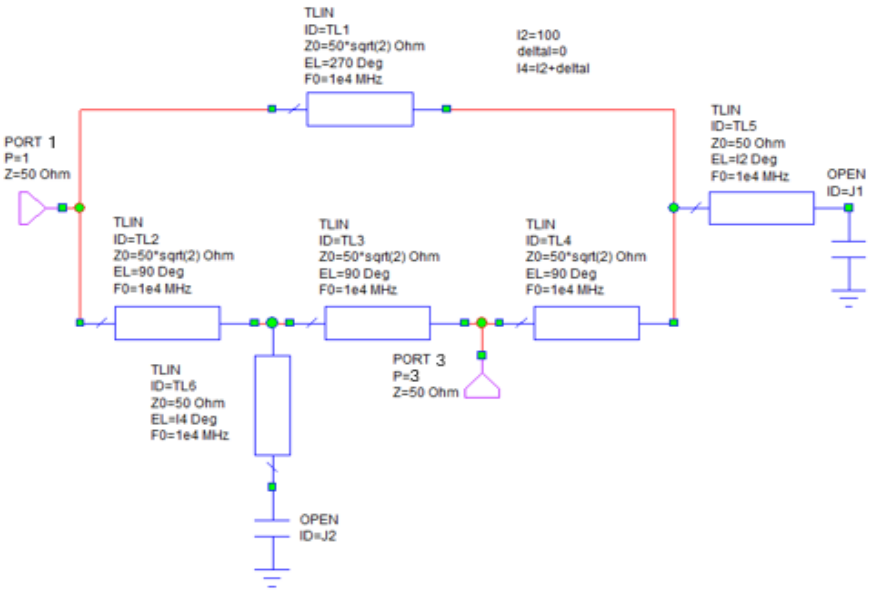

Figure 2.6 – Simple scheme of the rat-race sensor, using linear transmission lines.

Using microstrips, the difference of electrical length is produced employing materials with different dielectric properties, specifically different relative dielectric constants ε_r. In this way, a rat-race scheme was drawn using microstrip lines whose substrates have different ε_r. The width of the line depends on the impedance, which is 50Ω at the ports and $50\sqrt{2}\Omega$ in the ring; the length, only in the ring, depends on the wavelength, therefore on the frequency. In this regard, the choice of the central frequency depends on the relationship between the length and the width of the lines. Hence, to obtain strips not too large with respect to their length, the central frequency was fixed around 2.45 GHz.

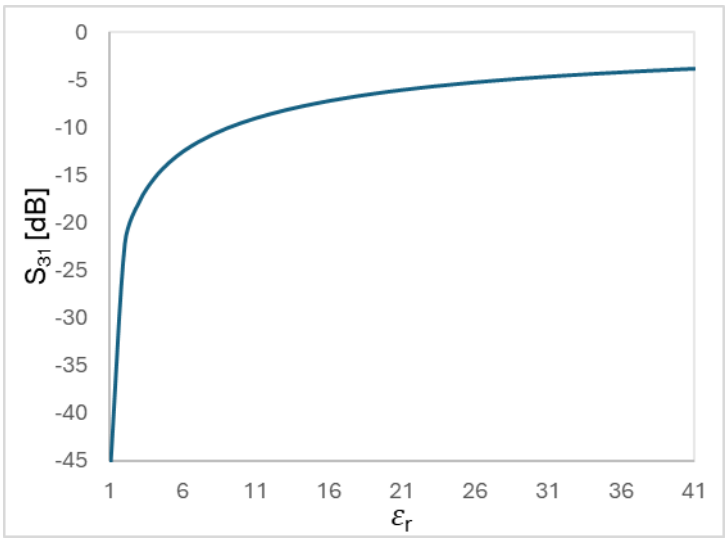

Figure 2.7 – Expected behaviour at the central frequency of the magnitude of S_{31} of the sensor at the variation of ε_r in port 4, when $\varepsilon_r = 1$ in port 2.

In the Figure 2.7 is shown the expected behaviour at the central frequency of S_{31}, when ε_r is equal to 1 at port 2 and varies at port 4. The magnitude of S_{31} is extremely low (ideally zero) when the relative dielectric constants at the two ports are both equal to 1, then it grows very rapidly for values of ε_r at port 4 close to 1 and tends to flatten when the constant is far from 1.

When the ε_r at port 2 is fixed at a higher value, the expected behaviour of the amplitude of S_{31} at the central frequency is like that is depicted in Figure 2.8a, in which is shown the example in which the relative dielectric constant at port 2 is fixed at 10. Also in this situation, the magnitude of S_{31} reaches its minimum when the dielectric constants are the same. So, it is possible to say that when the values of ε_r at port 2 and 4 are equal, S_{31} is ideally zero.

In case the fixed value of ε_r is 1, it will be possible to recognize the relative dielectric constant just measuring the magnitude of S_{31}. In case the fixed value is higher, the same value of S_{31} corresponds to two different values of ε_r, thus it will

be necessary to also know the phase to delete the ambiguity (in Figure 2.8b, there is a zoom around the value of the relative permittivity).

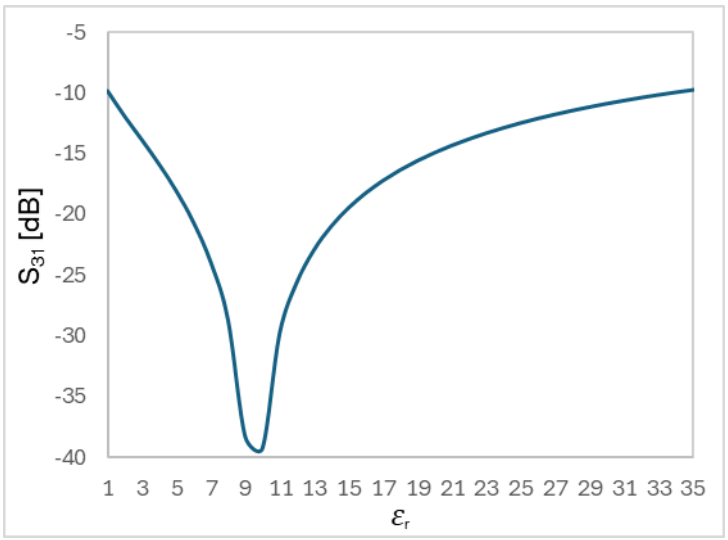

a)

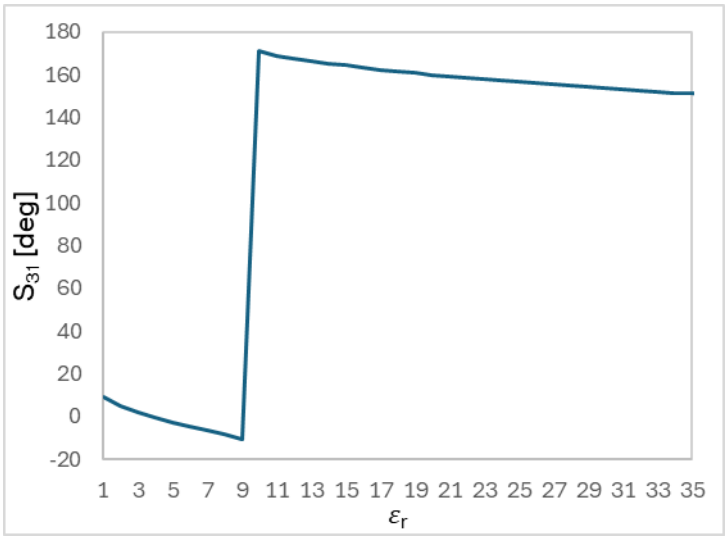

b)

Figure 2.8 – Expected behaviour at the central frequency of S_{31} of the sensor at the variation of ε_r in port 4, when $\varepsilon_r = 10$ in port 2: (*a*) magnitude and (*b*) phase.

2.5 Rectangular rat-race

Once the operative principle has been defined, the design of the sensor continues employing the Ansys HFSS Software.

The initial choice for the sensor design is to realize a rectangular-shaped rat-race, as illustrated in Figure 2.9.

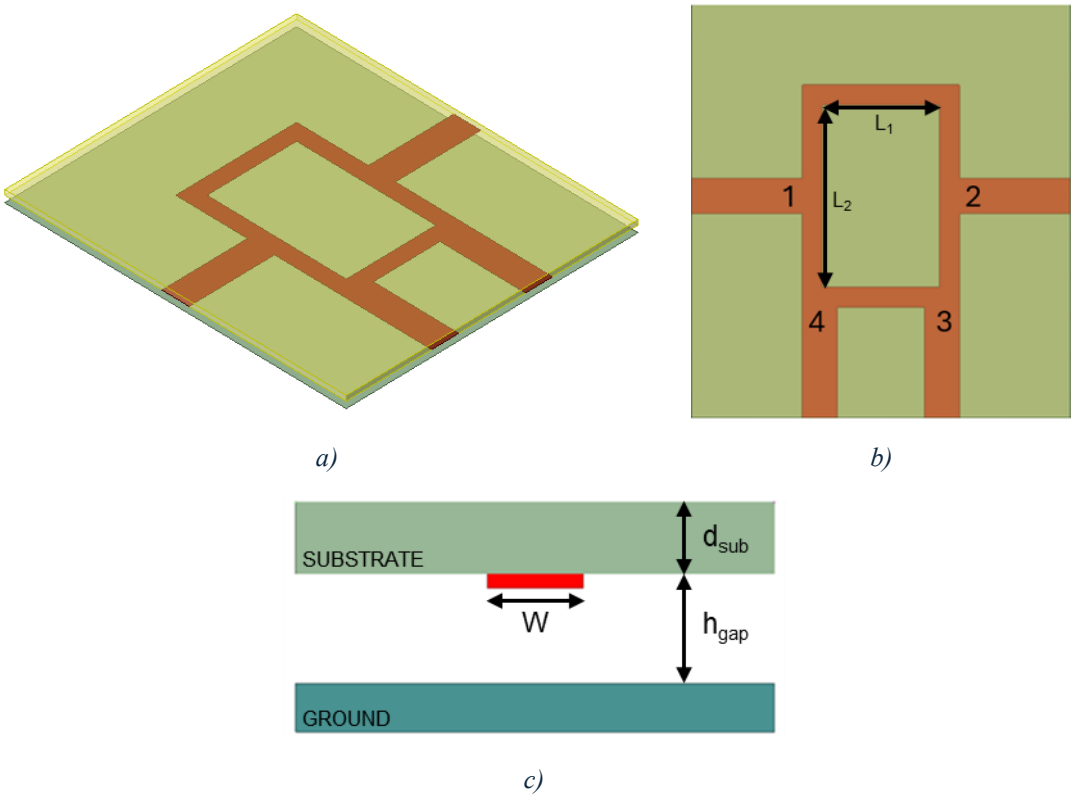

a) *b)*

c)

Figure 2.9 - Rectangular rat-race layout (*a, b*) with a section of the inverted microstrip line (*c*).

In this configuration, referring at the Figure 2.9b, port 1 is on the left and the other ones are set clockwise. The ring inner sides dimensions are L_1 = 28.9 mm and L_2 = 44.9 mm. The substrate is realized with Taconic RF-35 (ε_r = 3.5); looking at the Figure 2.9c, it has a thickness d_{sub} = 1.505 mm, and it is positioned above the ground plane at a distance h_{gap} = 2 mm. The 50Ω line sections have a width W of 8.68 mm while, in the $50\sqrt{2}\Omega$ section, W is 5 mm.

The Figure 2.10 shows the simulation results about the behaviour of the scattering parameters S_{11}, S_{21}, S_{31}, S_{41}. As it is possible to see, around the central frequency of 2.45 GHz, S_{11} and S_{31} are extremely low, while S_{21} and S_{41} have values around -3 dB. Thus, around the central frequency, the power that enters from port 1 is almost equally split between ports 2 and 4.

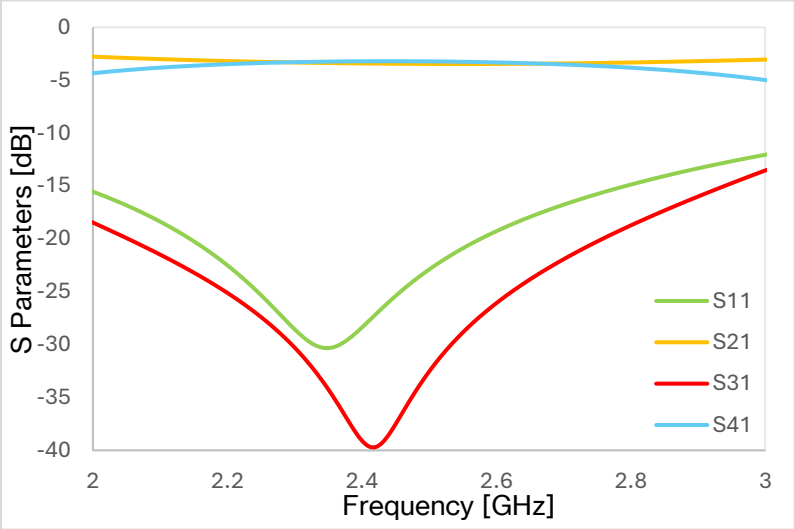

Figure 2.10 – Simulation of the frequency response of the scattering parameters for rectangular rat-race.

After the realization of the rat-race layout, there are added the open line section at ports 2 and 4, through open stubs, and the containers holding the samples, positioned under the stubs, as in Figure 2.11. The containers are made of plastic, with a relative dielectric constant of 2.25.

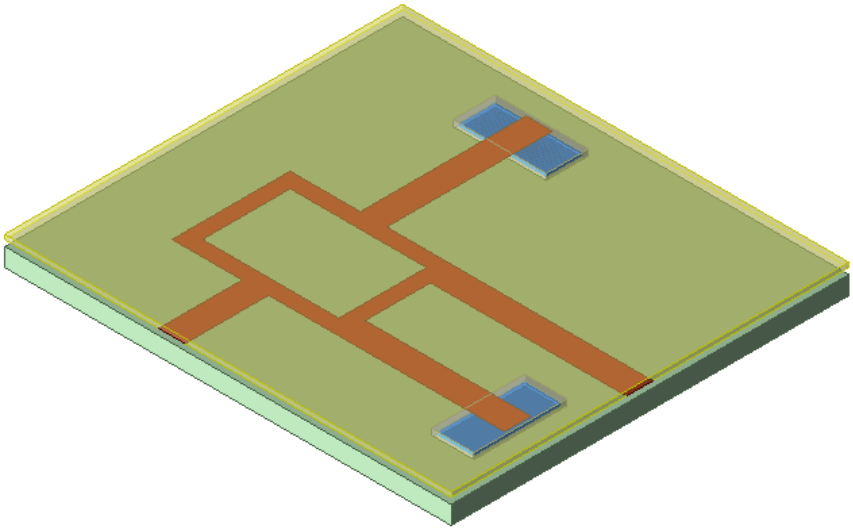

Figure 2.11 – Rectangular rat-race configuration with the samples inside the containers under the open stubs.

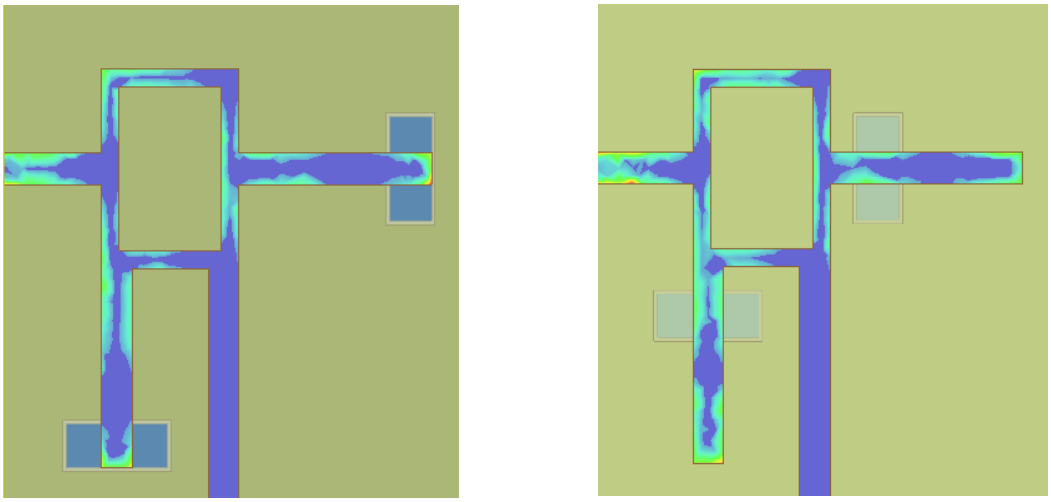

a) *b)*

Figure 2.12 – Simulation of the electric field distribution inside the strip in the rectangular rat-race configuration.

The length of the stubs depends on the electric field distribution. The idea is to place the containers where the electric field is more intense, to have stronger interactions between the dielectrics and the field, as depicted in Figure 2.12a, where the samples are positioned at the end of the stubs.

The field distribution depends on the standing waves, that are more intense at specific points. So, it is possible to put the samples closer to the coupler, as reported in Figure 2.12b.

Moreover, to downsize the sensor, another solution is to reduce the length of the branches, such in the example shown in the Figure 2.13a. Here, the length of the stubs is 7.5 mm from the outer side of the ring strip to the end.

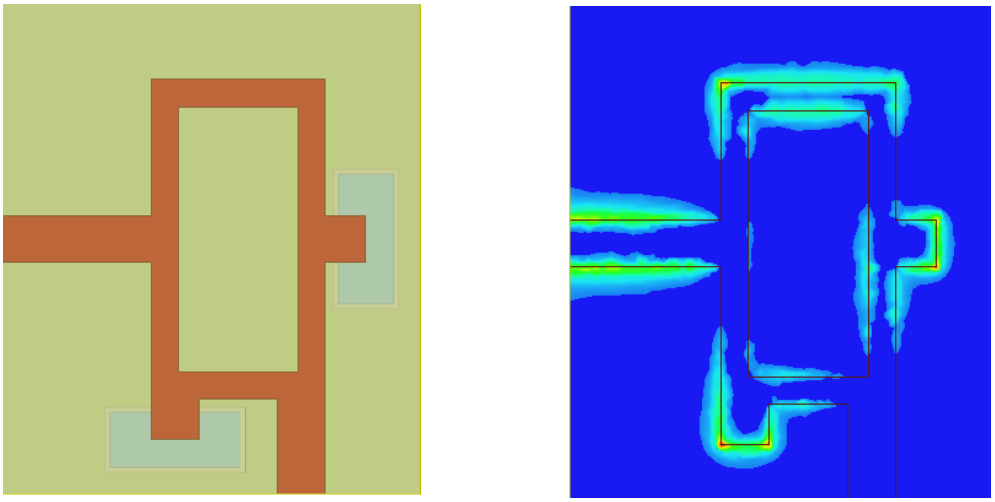

a) *b)*

Figure 2.13 – Example of a rectangular rat-race sensor with shorter open stubs: (*a*) layout; (*b*) simulation of the electric field distribution.

Analysing these configurations, the results are slightly different from what it is expected, because, in some conditions, the frequency response exhibits some undesired resonances, which alter the ε_r - S_{31} diagram at the central frequency. This phenomenon is manifested by the presence, in the frequency response, of some double peaks that converge at frequencies not much far from the central one. The reason is that the internal structure of the rat-race has not the correct dimensions, so it results unbalanced. The resonances are more noticeable when a sample with a higher ε_r is fixed. Specifically, if the sample is fixed at port 2, the double peaks appear when the sample at port 4 has a low value, while if the sample

is fixed at port 4, they appear when the other sample has a high value. In Figure 2.14a, it is reported an example, in which the sample is fixed at port 2 (in this case, $\varepsilon_r = 10$): the double peaks appear when ε_r is low, then they converge. Nevertheless, there is not a clear trend between the curves and the value of permittivity. The consequence is that the ε_r - S_{31} diagram at the central frequency does not present the expected minimum, as in Figure 2.8a, but it has a more disturbed behaviour, as plotted in Figure 2.14b.

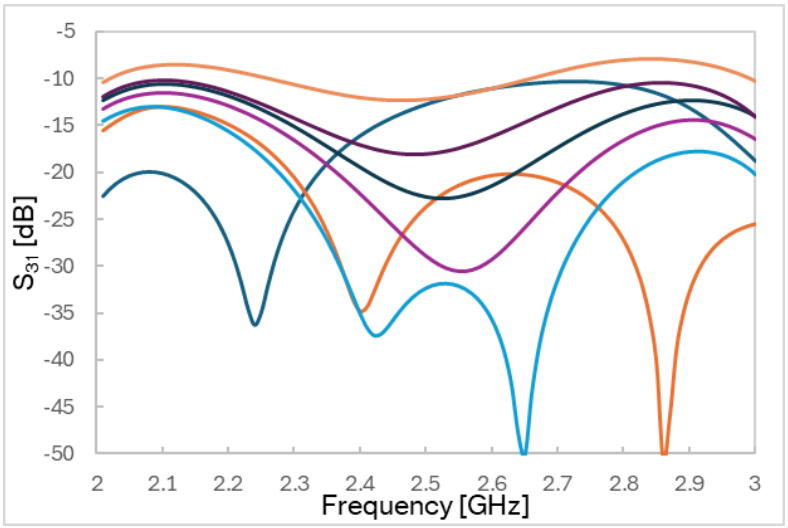

a)

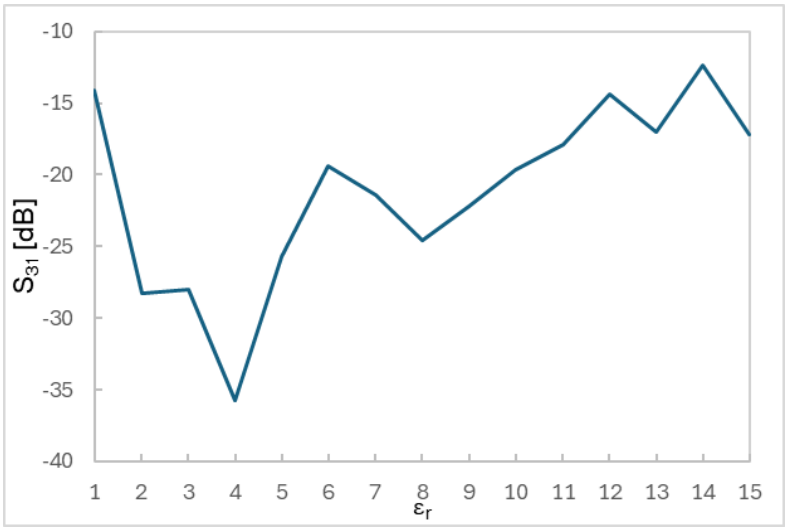

b)

Figure 2.14 - Example of frequency response of the rectangular configuration, when the reference sample has a $\varepsilon_r = 10$: (*a*) frequency sweep; (*b*) transmission levels at the central frequency.

To prevent this performance, the layout of the sensor is modified, passing from a rectangular configuration to a circular one. From this kind of structure, it is expected a better behaviour, because it is characterized by an axial symmetry, which guarantees the correct electric length among all output ports.

2.6 Circular rat-race

The sensor created with the circular rat-race configuration follows the rectangular layout, in terms of ports positioning and phase shift between each one. In fact, as shown in the Figure 2.15, if port 1 is located on the left of the ring, port 2 is on the right, so that 180° away from port 1. From port 2, in clockwise direction, port 3 is positioned 60° away, and port 4 120° away. To guarantee the electrical lengths of the rat-race coupler (270° between port 1 and 2, 90° between each of the other ones), the internal radius of the ring measures 24.7 mm. Moreover, the substrate, made of Taconic TLY (which has a relative permittivity of 2.2), is 60 mil (1.524 mm) thick. As the previous configuration, the 50Ω line sections (at the ports) has a width of 8.68 mm, while the $50\sqrt{2}\Omega$ section (the ring) is 5 mm wide.

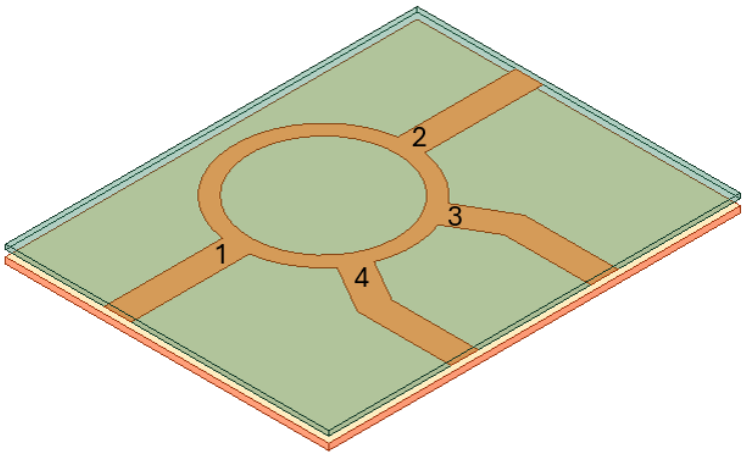

Figure 2.15 – Circular rat-race layout.

From this structure, it is possible to determine the position of the samples and the length of the stubs.

Specifically, the samples occupy a volume of 20 x 10 x 1.5 mm, and they are enclosed inside containers made of plastic (ε_r = 2.25), which have walls 1 mm thick. These dimensions are related to the minimum quantity of liquid necessary to obtain a noticeable interaction between the samples and the electric field.

Considering the strength of the electric field, the containers are placed close to the ring at port 2 and 4. The stubs, 5 mm wide, have their end in the region above the edge of the boxes: making simulations, it was chosen the final length, that is 14.5 mm from the centre of the ring strip to the end (Figure 2.16). With this length, at the central frequency, the magnitude of S_{31} appears to have a more pronounced peak around the considered permittivity.

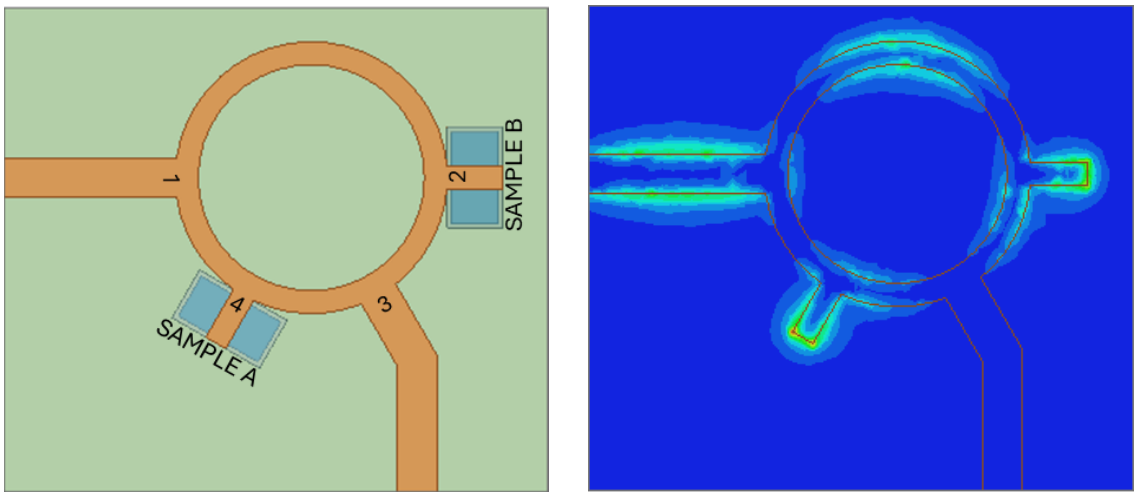

a) *b)*

Figure 2.16 - Final layout of the sensor (*a*), with electric field distribution (*b*).

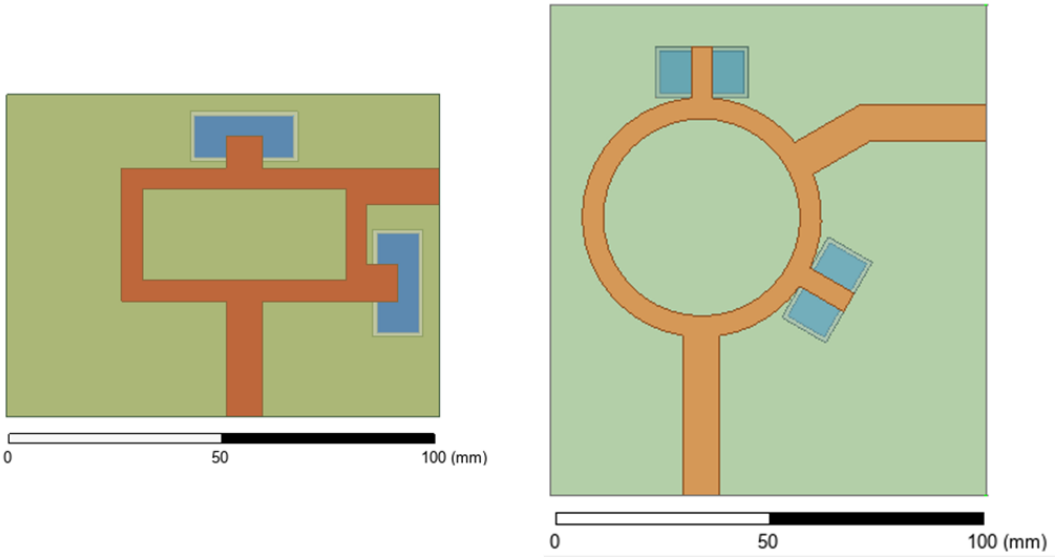

Figure 2.17 – Comparison between the areas occupied by the rectangular and the circular configurations.

Finally, in Figure 2.17, it is made a comparison between rectangular and circular configurations, in terms of area occupied by the sensor. The area of the rectangular rat-race is 21.35 cm^2, while in the circular one, it is 27.7 cm^2. The rings have not particularly different dimensions, but, in the first configuration, the shape helps to reduce the overall size of the sensor with respect to the other one.

2.7 Analytical study of the component

Once the model of the structure is obtained, the following step is to evaluate its functioning.

Calling the liquid samples inserted in the containers at port 4 and 2 ‘Sample A’ and ‘Sample B’, respectively (as indicated in Figure 2.16a), there are considered two specular conditions: in the first one, Sample A is a calibration liquid with known properties and Sample B changes, while, in the second one, Sample B is fixed and Sample A changes. In both cases, the considered values of relative dielectric constant of the calibration liquid are: 1, 3, 5, 10, 15 and 20. Since this analysis does not account for losses, the dielectric loss tangent is always null. In general, we expect analogous results from both situations.

2.7.1 Sample A is the calibration liquid

When Sample A is the calibration liquid, it is initially considered the situation in which Sample A has a relative permittivity ε_{rA} equal to 1.

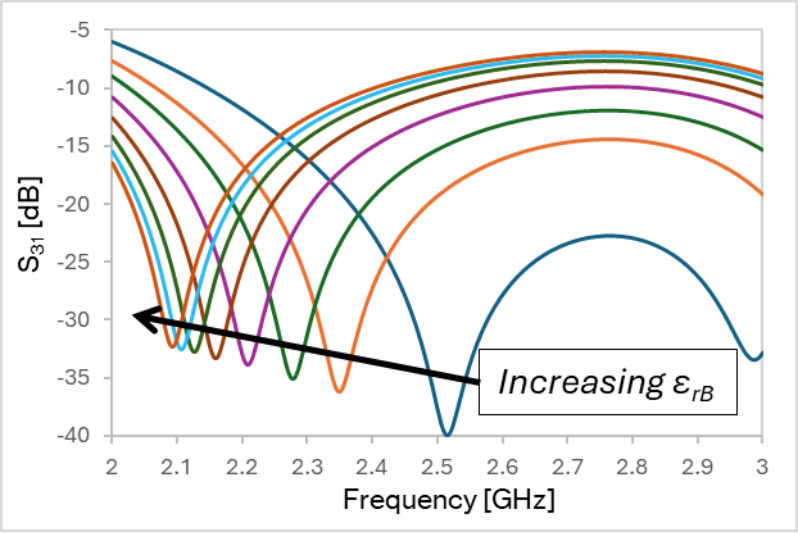

a)

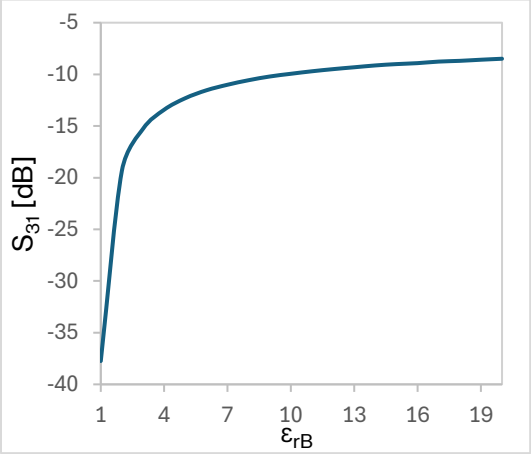

b)

Figure 2.18 – Magnitude of S_{31} when ε_{rA} = 1 and ε_{rB} is variable: (*a*) frequency response; (*b*) transmission levels at the central frequency of 2.5 GHz.

Referring to the graphs in Figure 2.18, the scattering parameter S_{31} changes its magnitude to the variation of the dielectric constant of Sample B (ε_{rB}). In Figure

2.18a, each trace corresponds to the variation in frequency of S_{31}, between 2 GHz and 3 GHz, for a variable value of ε_{rB}. It can be noticed that, for $\varepsilon_{rB} = 1$, a resonant negative peak occurs around 2.5 GHz, the chosen central frequency. Then, when the permittivity grows, the resonant peak occurs at lower frequencies, as indicated in the graph: in particular, for permittivity values close to 1, the frequency of the minima changes more rapidly, while, for bigger values of ε_{rB}, the position of the minima changes very slightly. Placing at the central frequency, as reported in Figure 2.18b, we observe that the magnitude of S_{31} changes vary rapidly for values of ε_{rB} close to 1, and very slightly for greater values, when the diagram appears almost flat.

Because the purpose of this sensor is to compare two liquid materials, the analysis is more significant when the comparison involves two samples with a similar relative permittivity. Therefore, for the following analysis, where ε_{rA} assumes higher values, the considered interval of ε_{rB} will be smaller than the situation when $\varepsilon_{rA} = 1$.

At this point, the analysis focuses on the case in which $\varepsilon_{rA} = 3$, concentrating on values of ε_{rB} between 1 and 5. The results are displayed in the graphs in Figure 2.19.

Studying the frequency response (Figure 2.19a), for values of ε_{rB} close to 1, there is a negative peak around 2.7 GHz, then the curves have two peaks moving away from each other. In particular, for frequencies lower than 2.7 GHz, the peak occurs at lower frequencies as the permittivity of Sample B increases and, when $\varepsilon_{rB} = \varepsilon_{rA}$, the negative peak is at the central frequency. Hence, it is possible to examine at which frequency occurs the minimum with respect the value of ε_{rB} (Figure 2.19b): in this case, the peaks happen at 2.7 GHz for permittivity values until 2.2, then the frequency decreases as the dielectric constant grows. Observing the transmission levels at 2.5 GHz (Figure 2.19c), it is noticed that, when the permittivity values of the samples are the same, the magnitude of S_{31} reaches its minimum.

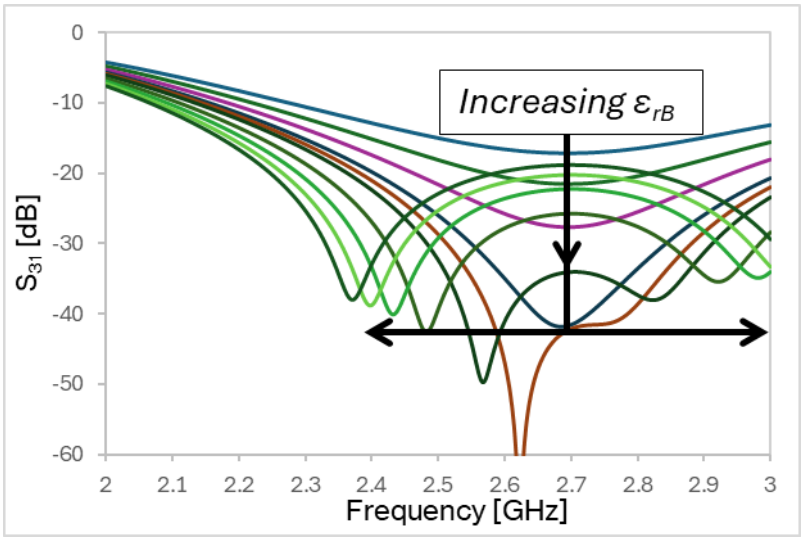

a)

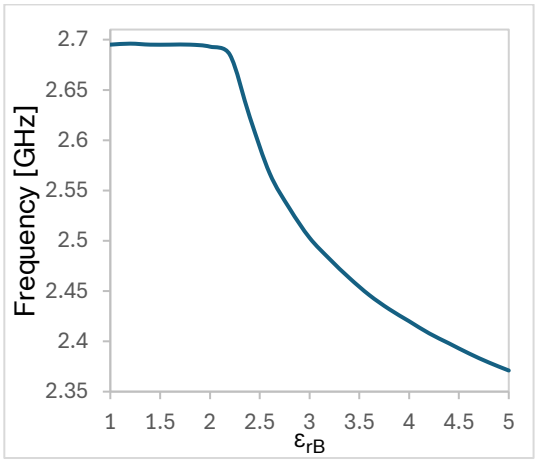

b)

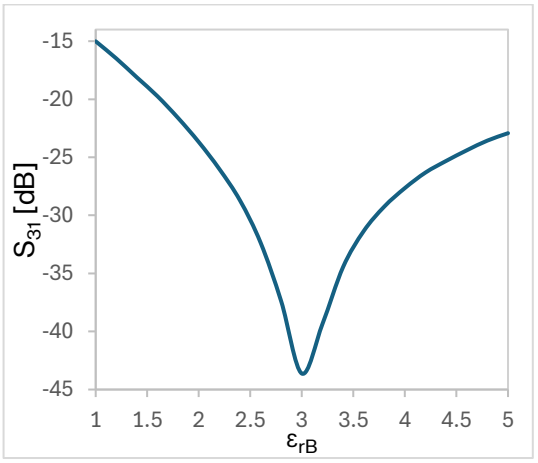

c)

Figure 2.19 – Situation when $\varepsilon_{rA} = 3$: (*a*) frequency response of S_{31}; (*b*) frequencies at the minima of S_{31}; (*c*) transmission levels of S_{31} at 2.5 GHz.

Now, we focus on the case in which $\varepsilon_{rA} = 5$, concentrating on values of ε_{rB} between 3 and 7. The results are reported in the graphs in Figure 2.20.

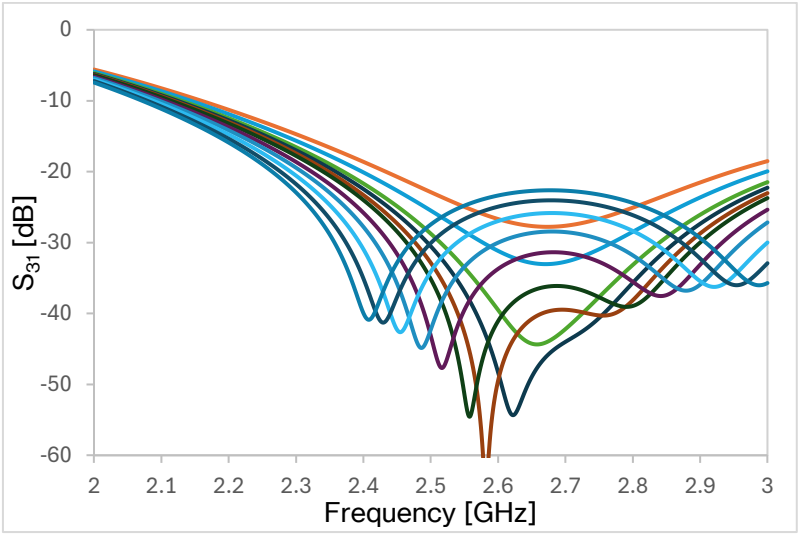

a)

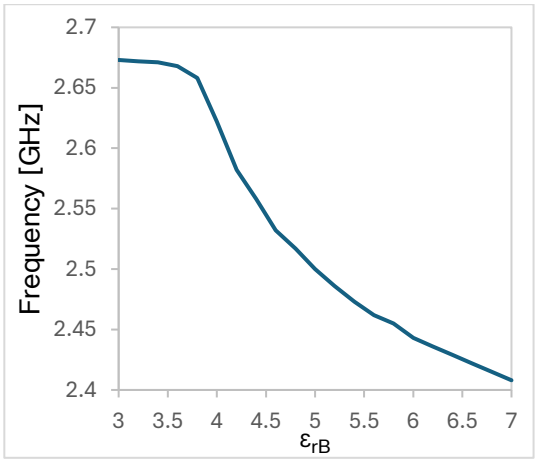

b)

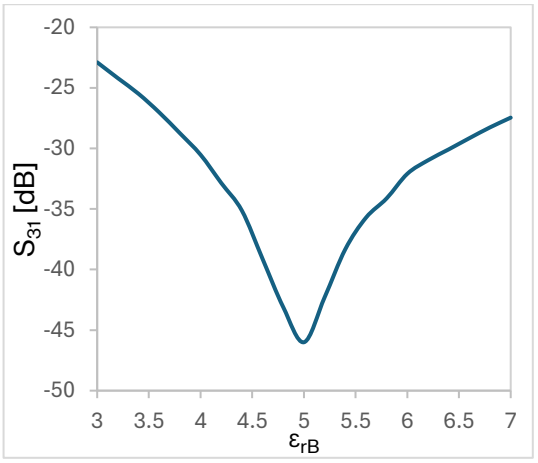

c)

Figure 2.20 - Situation when $\varepsilon_{rA} = 5$: (*a*) frequency response of S_{31}; (*b*) frequencies at the minima of S_{31}; (*c*) transmission levels of S_{31} at 2.5 GHz.

In Figure 2.20a, it is displayed the frequency response of the amplitude of S_{31}. The trend is similar to the previous case, but for the curves with double peaks, these ones begin to get closer in frequency. Moreover, looking at the Figure 2.20b, also the interval of frequencies in which the minima occur is narrower, maintaining a descendent attitude. In Figure 2.20c, there is the trend of the magnitude of S_{31} compared with permittivity at the central frequency, which still shows the minimum when the permittivity of Sample B is equal to that of Sample A. It is

possible to notice that the peak is slightly less narrow than the previous case: this is because the absolute difference between the permittivity values is the same, but the relative difference is smaller, so the variation of the magnitude of S_{31} diminishes inside a fixed interval of ε_{rB}.

In Figure 2.21, there are reported the results for the case in which $\varepsilon_{rA} = 10$, for ε_{rB} between 8 and 12.

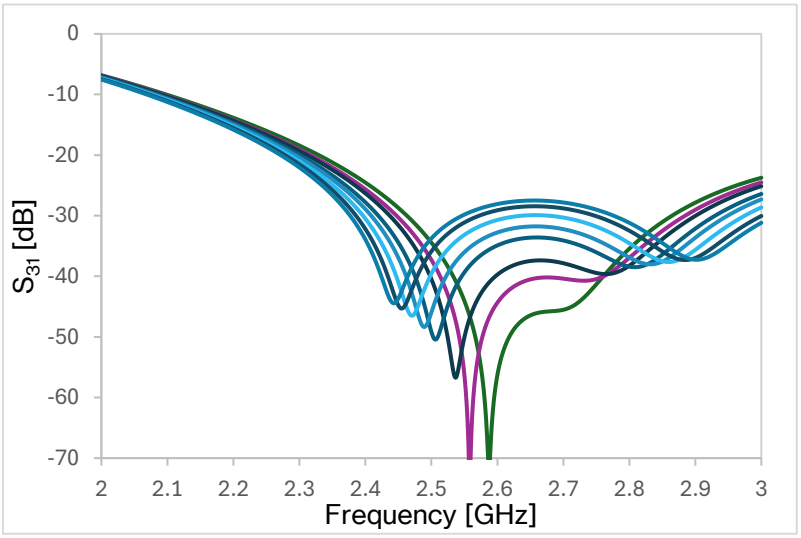

a)

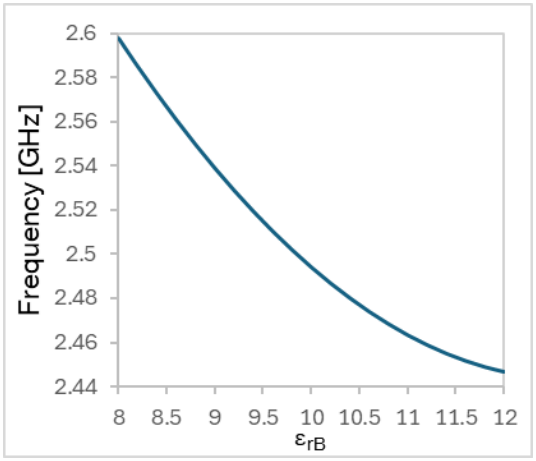

b)

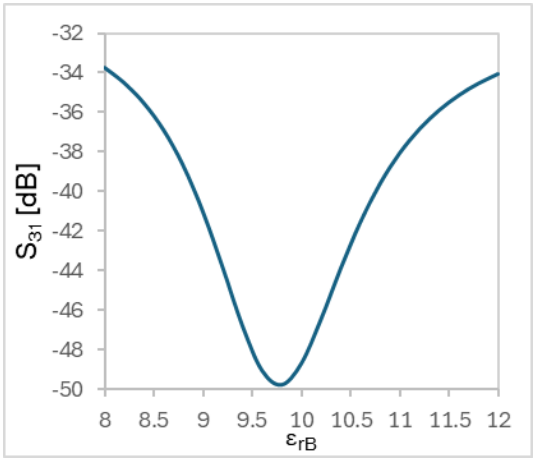

c)

Figure 2.21 - Situation when $\varepsilon_{rA} = 10$: (*a*) frequency response of S_{31}; (*b*) frequencies at the minima of S_{31}; (*c*) transmission levels of S_{31} at 2.5 GHz.

Looking at the graphs, it is possible to observe that the minimum values of the curves (Figure 2.21a) change quite rapidly with ε_{rB}. Moreover, as detectable in Figure 2.21c, a left shift affects the peak of the magnitudes at 2.5 GHz, that no longer occurs when the relative dielectric constants of the two samples are exactly equal. This shift, in addition to the change in the attenuation peak depending on the material (as visible in Fig. 2.21a), happens because high values of ε_r have a slight effect on the total electrical length of the rat-race, so the minimum peak tends to decrease in frequency when the liquids are balanced. Finally, the phenomena of the reduced frequency range of the minima and the wider peak of the transmission levels at the central frequency are enhanced.

The trend seen in the last case continues when the relative dielectric constant of Sample A grows further, as it is possible to observe in Figures 2.22 and 2.23, where there are illustrated the results of the simulations for ε_{rA} equal to 15 and 20.

Since the relative variation of ε_{rB} becomes smaller as the fixed value of ε_{rA} grows, if we observe the frequency responses (Fig. 2.22a, 2.22b), the curves tend almost to overlap in frequency. Consequently, the frequency range of the minima tends to reduce, as plotted in Figures 2.23a and 2.23b. Finally, looking at the Figures 2.23c and 2.23d, the peak of the minimum transmission level at the central frequency continues to move left as ε_{rA} increases.

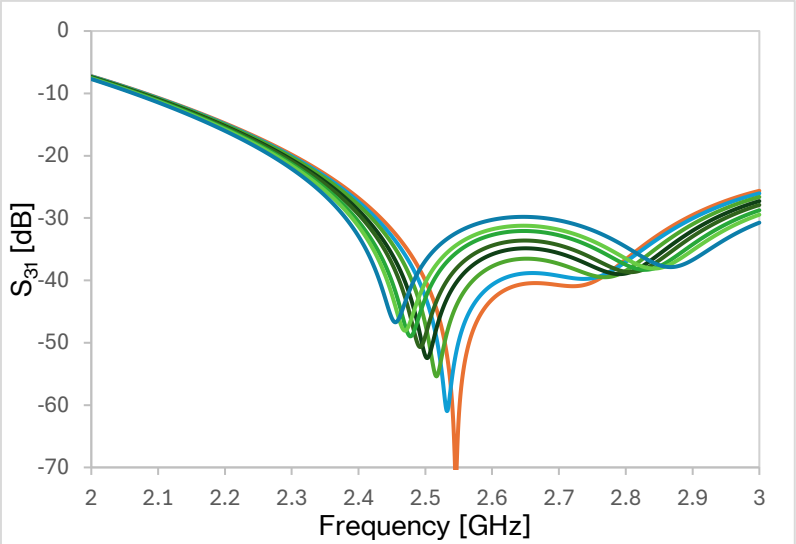

a)

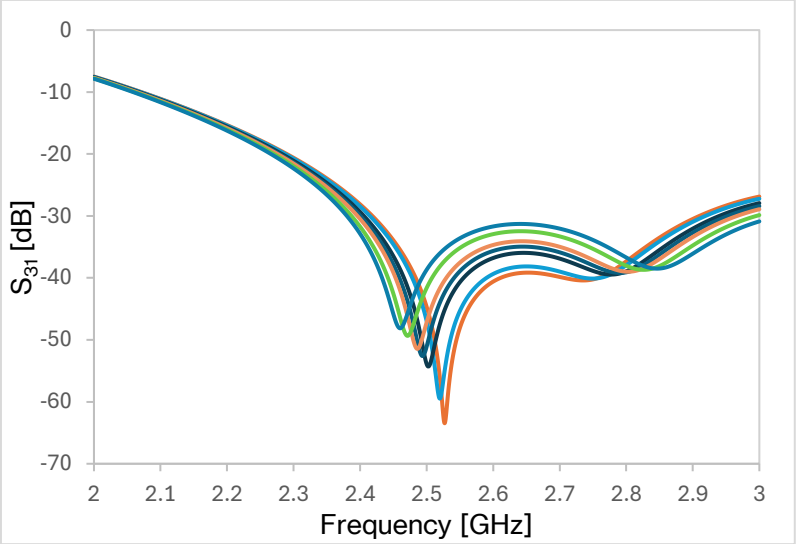

b)

Figure 2.22 - Frequency response of S_{31} when ε_{rA} is fixed at 15 (*a*) and 20 (*b*).

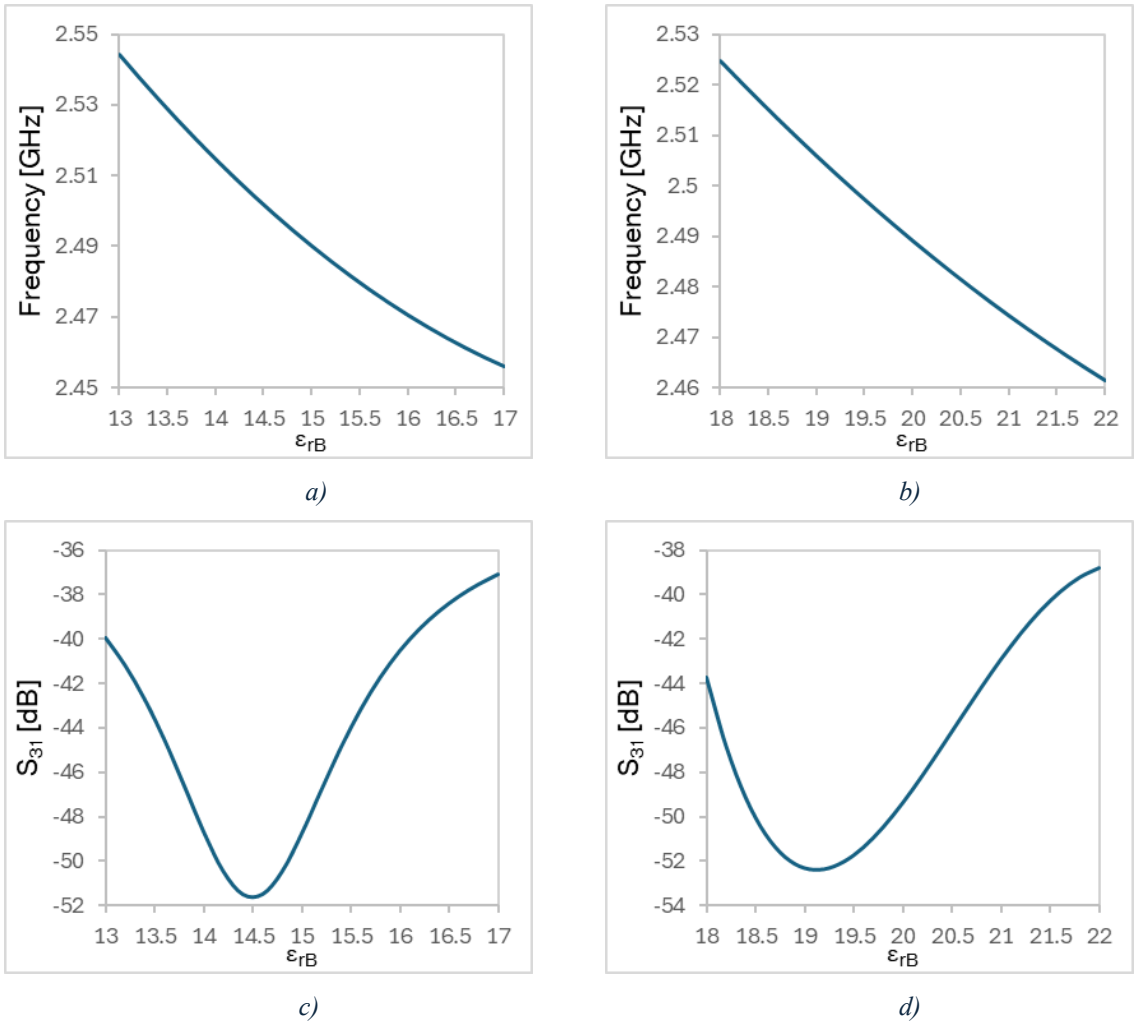

Figure 2.23 - Frequencies at the minima of S_{31} when ε_{rA} is fixed at 15 (*a*) and 20 (*b*); transmission levels of S_{31} at 2.5 GHz when ε_{rA} is fixed at 15 (*c*) and 20 (*d*).

2.7.2 Sample B is the calibration liquid

At this point, the analysis passes to the conditions in which Sample B is the calibration liquid, making also comparisons with the opposite situation.

When ε_{rB} is 1, the performance of the magnitude of the scattering parameter S_{31} shows, around the central frequency, a resonant negative peak only when $\varepsilon_{rA} = \varepsilon_{rB}$ (Figure 2.24a), differently from the condition where the calibration liquid is Sample A. At 2.5 GHz, the amplitude of S_{31} starts from an extremely low value when ε_{rA} is close to 1, then increases very rapidly and finally flattens for values of ε_{rA} far from 1. In Figure 2.24b, it is reported the comparison with the opposite situation: the trends are practically overlapping.

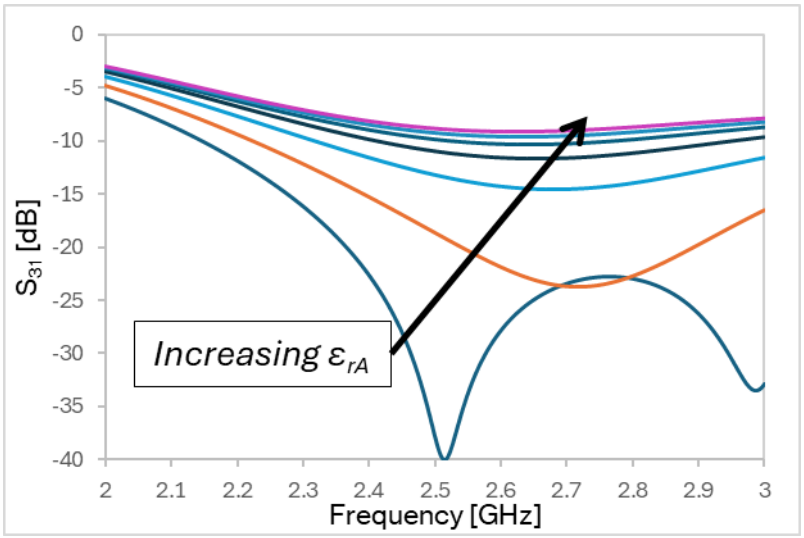

a)

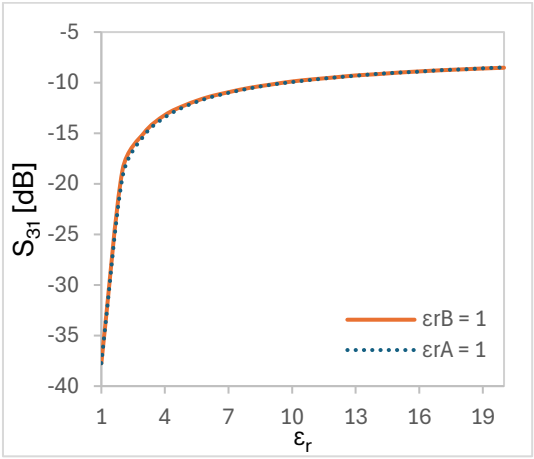

b)

Figure 2.24 - Magnitude of S_{31} when ε_{rB} = 1 and ε_{rA} is variable: (*a*) frequency response; (*b*) transmission levels at the central frequency of 2.5 GHz (and comparison with ε_{rA} = 1 and ε_{rB} variable).

When ε_{rB} is 3 (Figure 2.25), the behaviour of the frequency response is specular to the situation in which the other sample is fixed. So, starting from ε_{rA} = 1, there are two resonant peaks that come closer to each other as the relative dielectric constant increases, until, for a ε_{rA} around 4, these peaks combine with each other. This trend is related also to the results shown in the Figure 2.25b, where there are collected the frequencies at the minima related to ε_{rA}: here, it is visible the symmetry with respect to the case of fixed ε_{rA}, since the curve has now an

ascendent attitude. Moreover, at the central frequency, the curves cross each other when the permittivity is equal to 3. Finally, about the transmission levels at 2.5 GHz, comparing the two situations, it is still detectable an overlap between the curves, which have a peak in correspondence of equal dielectric constants.

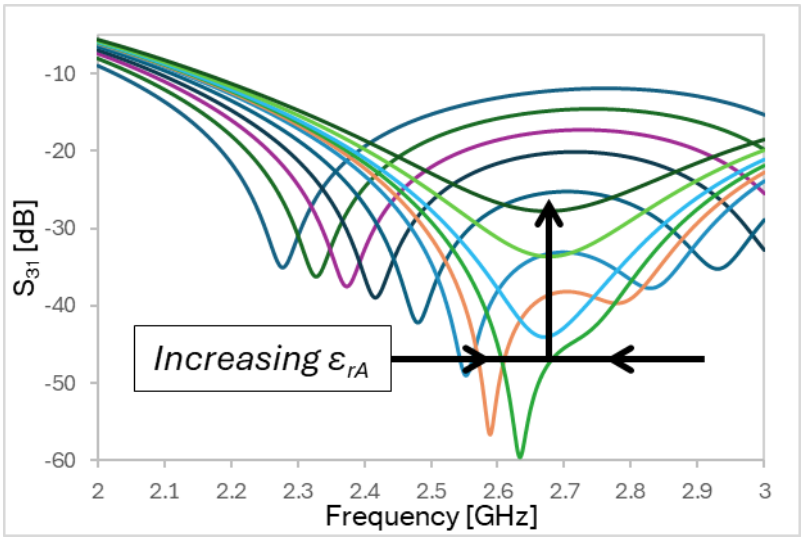

a)

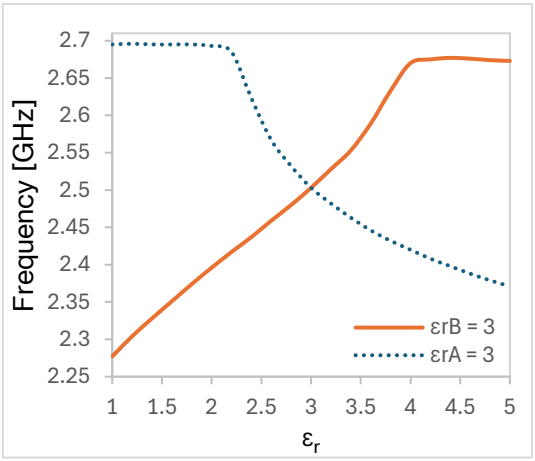

b)

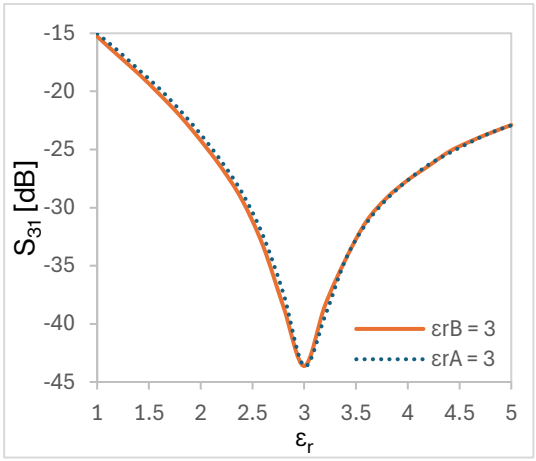

c)

Figure 2.25 - Situation when $\varepsilon_{rB} = 3$: (*a*) frequency response of S_{31}; (*b*) frequencies at the minima of S_{31}; (*c*) transmission levels of S_{31} at 2.5 GHz (and comparisons with $\varepsilon_{rA} = 3$ and ε_{rB} variable).

In a similar way, the sensor behaves if $\varepsilon_{rB} = 5$, with a smaller variation of the amplitude of S_{31} within the same absolute difference of relative dielectric constant. Also in this situation, the negative peak of the transmission levels happens when the value of $\varepsilon_{rA} = \varepsilon_{rB}$. However, comparing this outcome with the opposite

condition, the curves do not exactly overlap, but the current one is slightly right-shifted (Figure 2.26c).

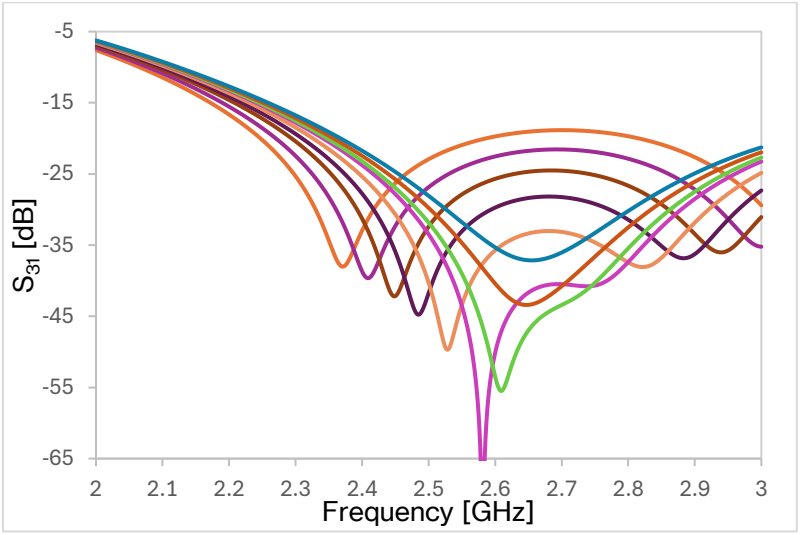

a)

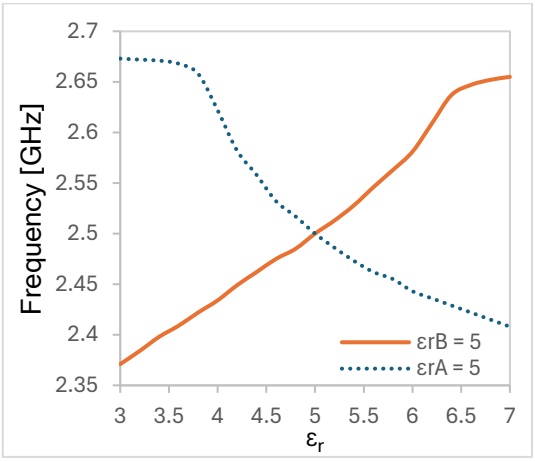

b)

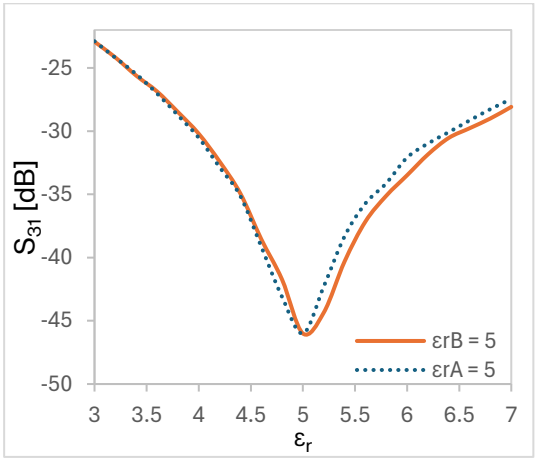

c)

Figure 2.26 - Situation when $\varepsilon_{rB} = 5$: (*a*) frequency response of S_{31}; (*b*) frequencies at the minima of S_{31}; (*c*) transmission levels of S_{31} at 2.5 GHz (and comparisons with $\varepsilon_{rA} = 5$ and ε_{rB} variable).

Increasing the value of ε_{rB}, as when Sample A is fixed, the resonant double peaks tend to get closer in frequency for each curve, so that the range of the frequencies at the minima is going to reduce. Taking the results plotted in Figure 2.27 (for ε_{rA} equal to 10 and 20), it is once more proved that if the fixed liquid has a higher value of relative dielectric constant, the absolute variation of the ε_r of the other sample will correspond to a less significant variation of it in relative terms.

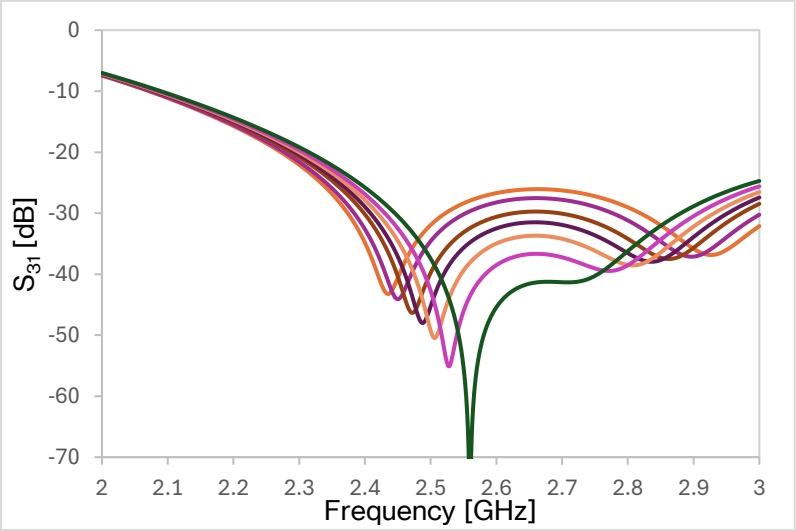

a)

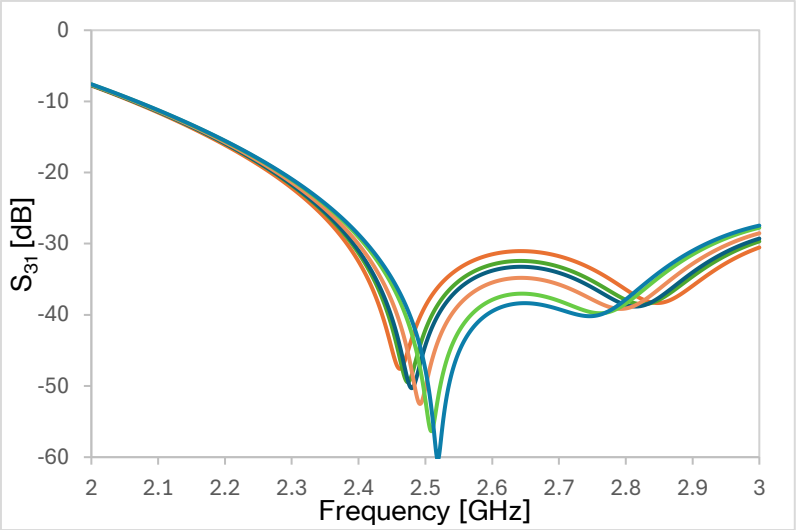

b)

Figure 2.27 – Frequency response of the amplitude of S_{31}, when ε_{rB} = 10 (*a*) and 20 (*b*).

Returning to the frequency range of the minima, the graphs displayed in Figures 2.28a, 2.28c, 2.28e confirm that, also in this configuration, increasing the fixed ε_r, the range of frequencies is narrower. Moreover, comparing with the previous configuration, it is possible to see that the intersection of the curves appears not exactly at the central frequency, but slightly shifted, especially for the cases in which ε_r is equal to 15 and 20. This occurrence coincides with the shift of the peaks of the minimum transmission level of S_{31} at the central frequency (Fig.

2.28b, 2.28d, 2.28f). When ε_{rB} is fixed, the peak tends to move right at the increase of ε_{rB}, differently from the other situation.

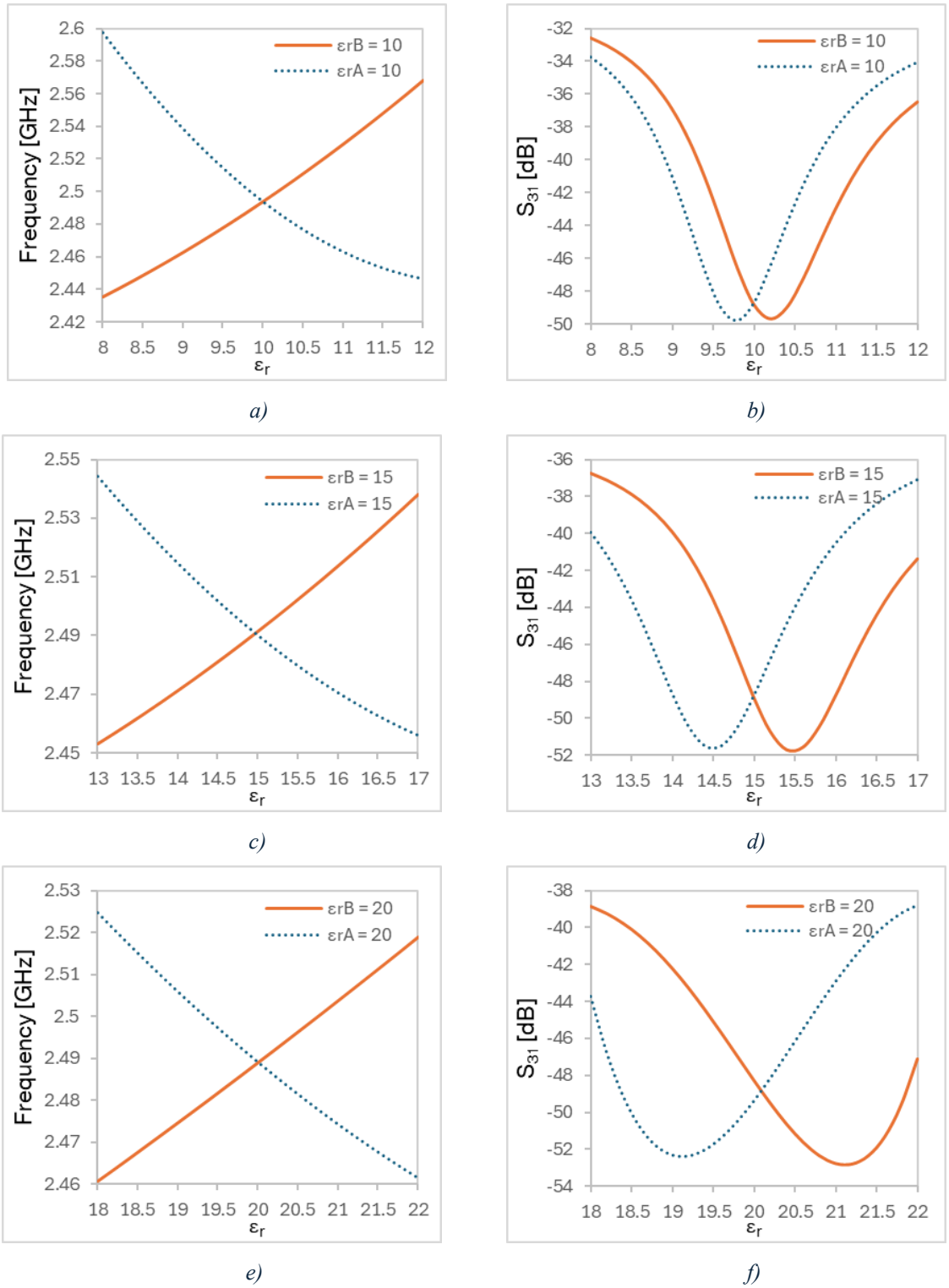

a) *b)*

c) *d)*

e) *f)*

Figure 2.28 – Frequencies at the minima of S_{31} for ε_{rB} = 10, 15, 20 (*a, c, e*); transmission levels of S_{31} at 2.5 GHz for ε_{rB} = 10, 15, 20 (*b, d, f*). Results compared with ε_{rA} = 10, 15, 20 and ε_{rB} variable.

Chapter 3

Fabrication and measurements of the sensor prototype

3.1 Fabrication of the prototype

Once completed the design and the analysis of the sensor, the following step is the fabrication of the prototype.

The sensor is assembled using a hybrid technology, in which a standard printed circuit board (PCB) is integrated with 3D printing. Specifically, the structure of the inverted microstrip (comprising the dielectric substrate with the metal strip) is realized using the PCB, while the containers and the support structure are made with a 3D printer. This hybrid technology permits to have several advantages. Thanks to the inverted microstrip, the device shows low losses and an easy connector mounting. The 3D printing adds a great design flexibility and accuracy, despite relatively low costs. Moreover, this solution gives the possibility to dismount and change pieces very easily [6].

Thanks to its properties, 3D printing technology has been widely used, in the last years, to develop different kinds of microwave devices, such as sensors, transitions and filters.

A sensor characterized by a resonant cavity based on SIW technology [4] has been fabricated by using a stereolithographic 3D printing. The solution based on a section of inverted microstrip line with a quarter wavelength open ended stub [6] has been realized with a hybrid technology (PCB-3D printing), as well as the device with an open-ended broadside-coupled-line section (laminate-3D printing)

[9]. In the solution consisting of two rectangular cavities [11], the cavity filter is 3D printed.

Other types of microwave devices can be the transitions from a microstrip on a PCB to a 3D printed metal-coated air-filled waveguide. They can be realized by sharing a common ground plane [16], or by using an additively manufactured radiation probe [17], or by employing a through-patch coupling interface [18].

Furthermore, there can be considered band-pass filters based on empty single-ridge waveguide [19], or on modified sections of this kind of waveguide [20]: the 3D printing provides a rapid manufacture of complex geometries at a very reduced price.

In Figure 3.1, there is depicted the pre-fabrication model, which includes the substrate, the ground support, the containers, the support feet to hold the substrate, the holes for the transitions (at ports 1 and 3, as depicted in Figure 3.2b) and the inlets/outlets for the liquid insertion inside the containers.

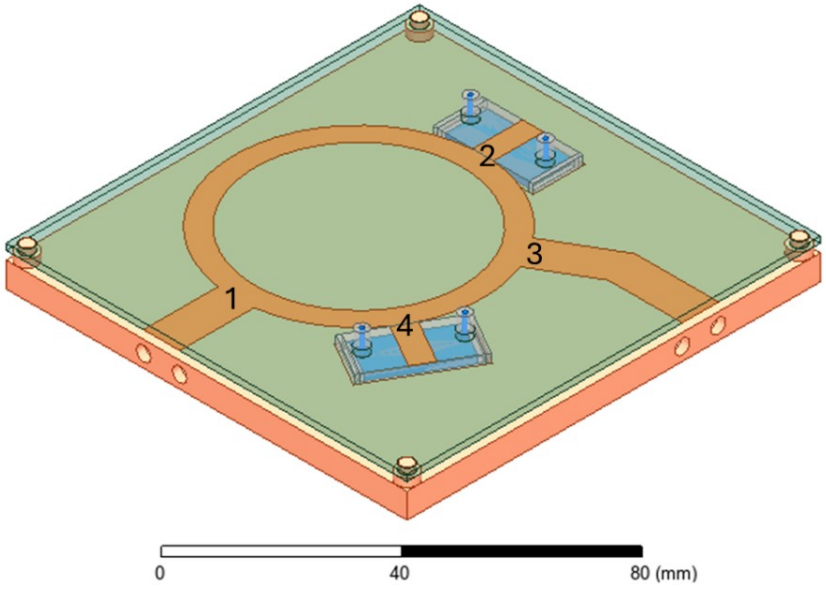

Figure 3.1 – Pre-fabrication model of the sensor prototype.

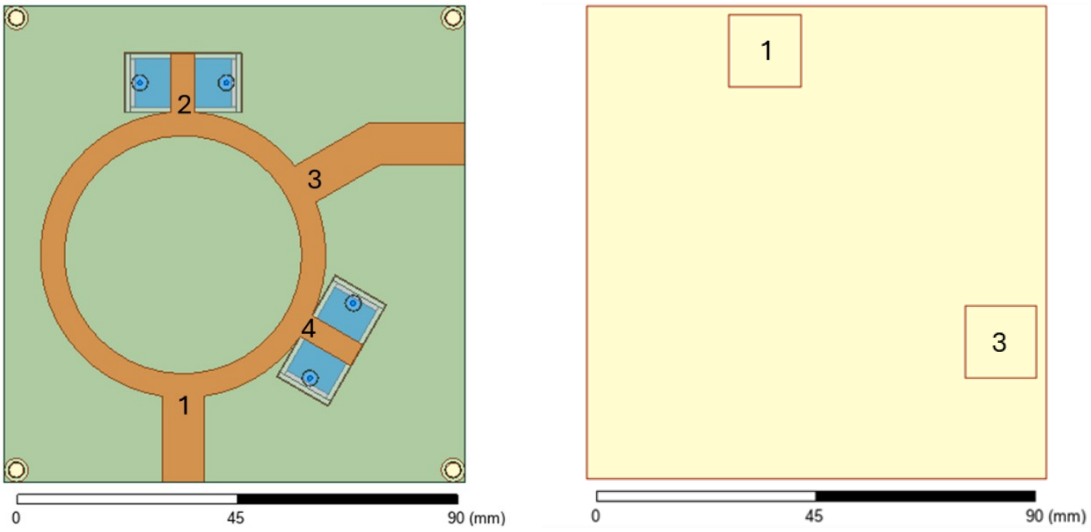

a) *b)*

Figure 3.2 – Pre-fabrication model of the sensor prototype: (*a*) top view; (*b*) bottom view.

The dielectric substrate used is the "Nelco NY9220" (ε_r = 2.2), and the inverted microstrip has been milled with the "LPKF Protomat E33" milling machine (Figure 3.3a). Input and output lines of the rat-race have been tapered, as visible in Figure 3.3b.

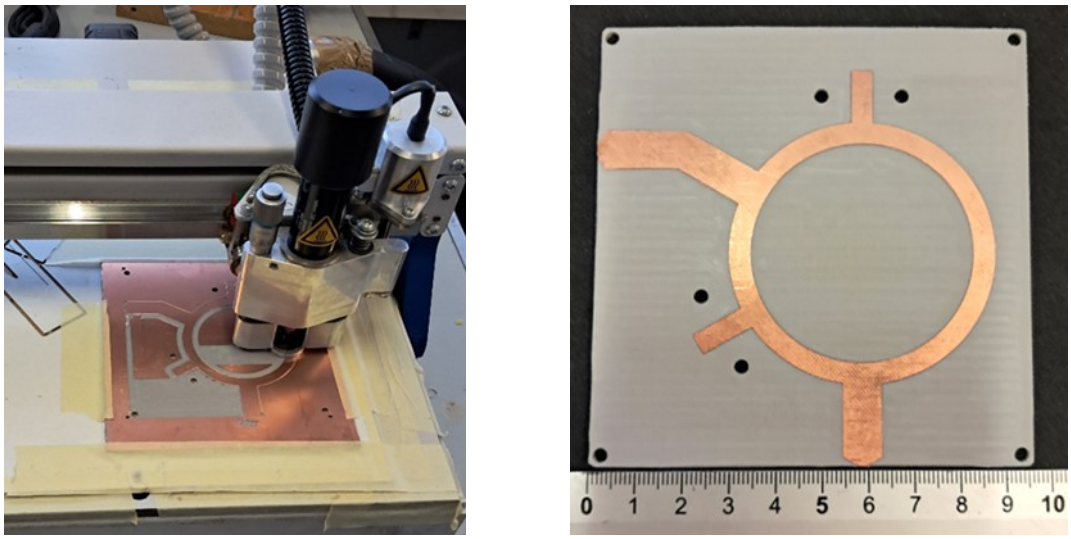

c) *b)*

Figure 3.3 – Dielectric substrate and metal strip of the inverted microstrip: (*a*) milling; (*b*) result.

The containers and the support structure of the device have been fabricated with a "Stratasys Objet500 Connex3" 3D printer, employing a specific polymer, the "Stratasys VeroWhite". Thanks to the 3D printing technology "PolyJet", it has been possible to get containers hollow inside, since the component is manufactured building a single block composed of two materials, a main polymer and a support one: the support material is partially water-soluble, and it is removed by immersion in a solvent. So, the single box has been produced in three pieces - the central body and two side caps - which later have been glued together, as shown in Figure 3.4.

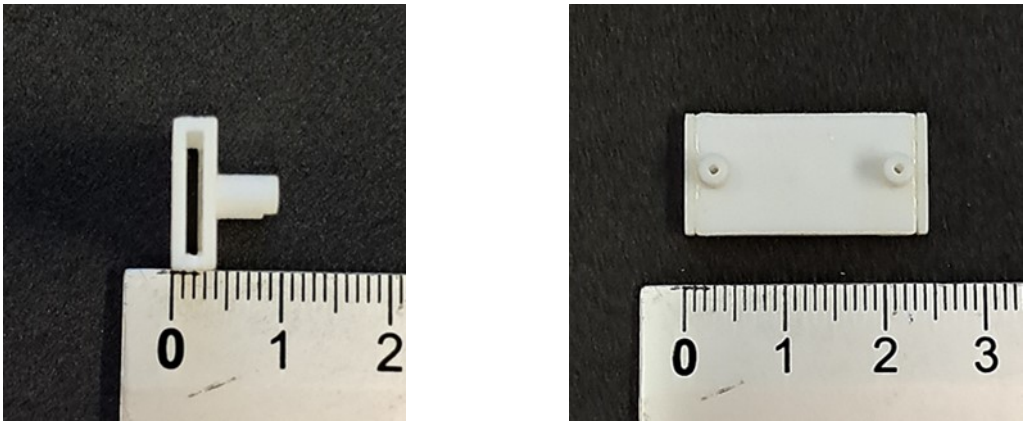

a) *b)*

Figure 3.4 – Container: (*a*) hollow section; (*b*) the final structure with the glued caps.

In Figure 3.5 is shown the ground support, which includes the support feet at each corner and the holes at the bottom side for the transition fixing. Moreover, on the top side, the surface appears partially excavated in the position in which the containers will be arranged: this happens because it is needed a compromise between the minimum height of the channel in which there will be the liquid sample and the distance between the ground and the metal strip.

In Figure 3.6, finally, an overview of the sensor's components is displayed.

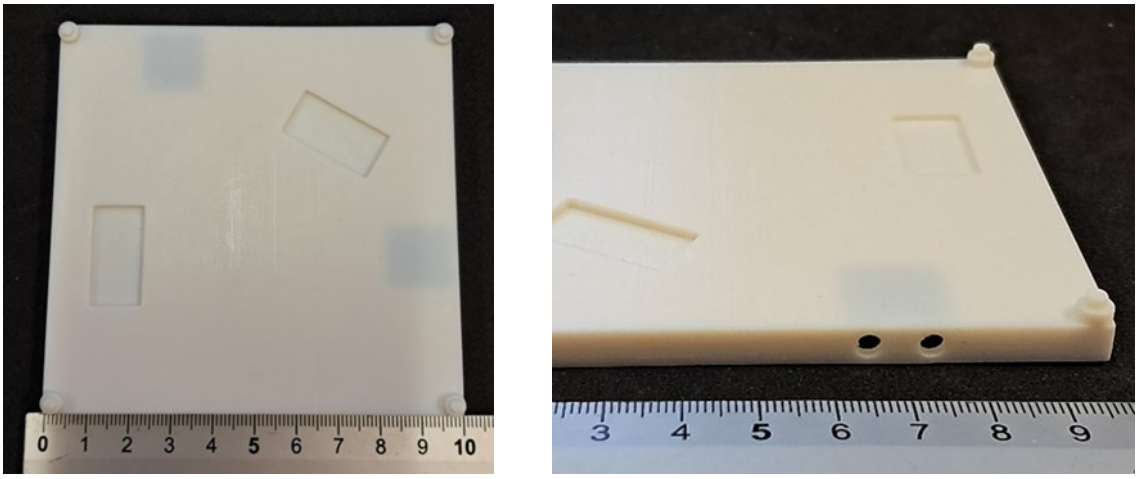

a) *b)*

Figure 3.5 – Ground support: (*a*) top side; (*b*) view on the holes for transition fixing.

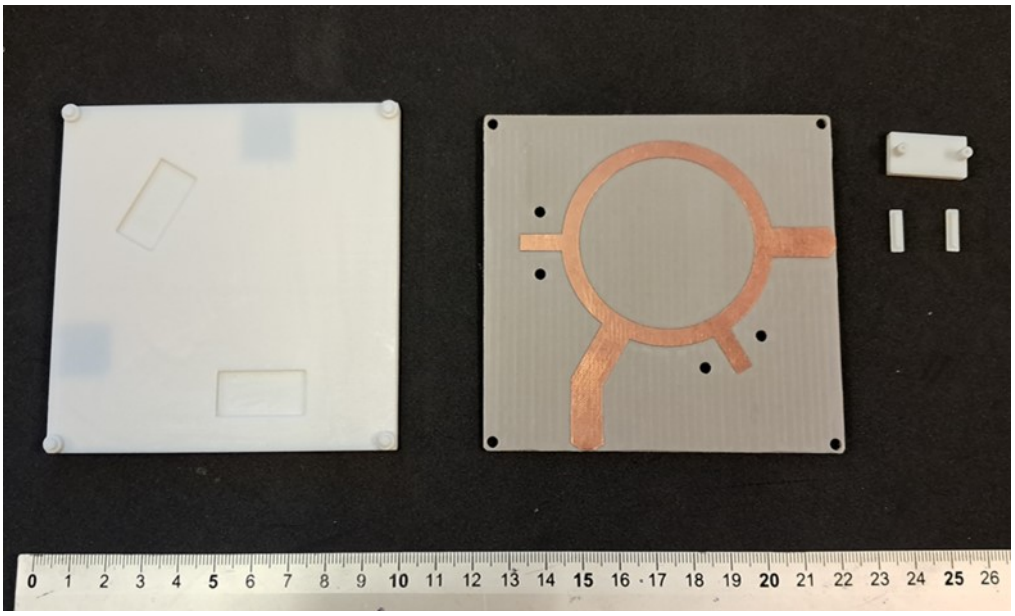

Figure 3.6 – Overview of the sensor's components.

The ground layer has been subsequently covered with a conductive paste, the "LPKF ProConduct", as reported in Figure 3.7.

After having placed the containers on the ground, the final step is to assembly the sensor, realize the transitions soldering SMA connectors to the metal strips at the

input and output ports, and then fix them with screws to the ground support. The result is displayed in Figure 3.8.

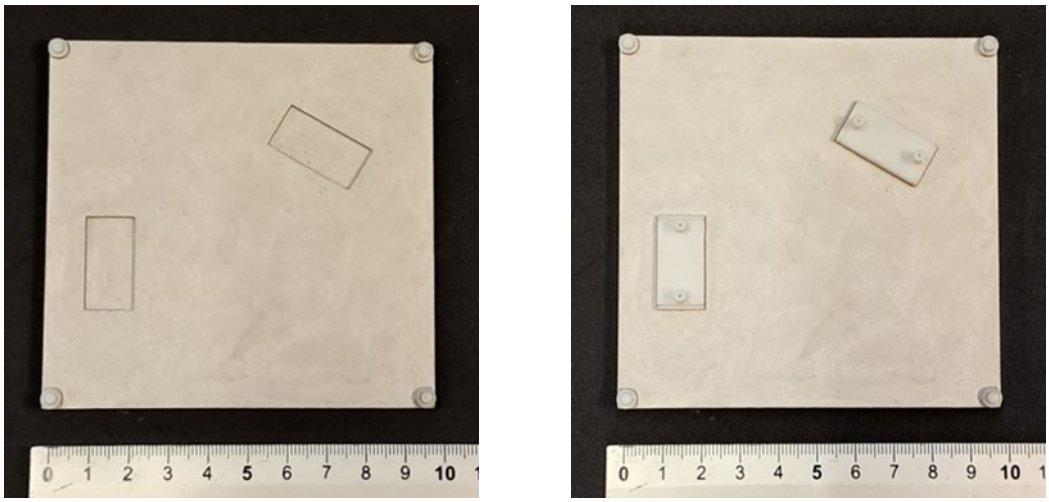

a) *b)*

Figure 3.7 – Ground layer covered with the conductive paste and the glued containers.

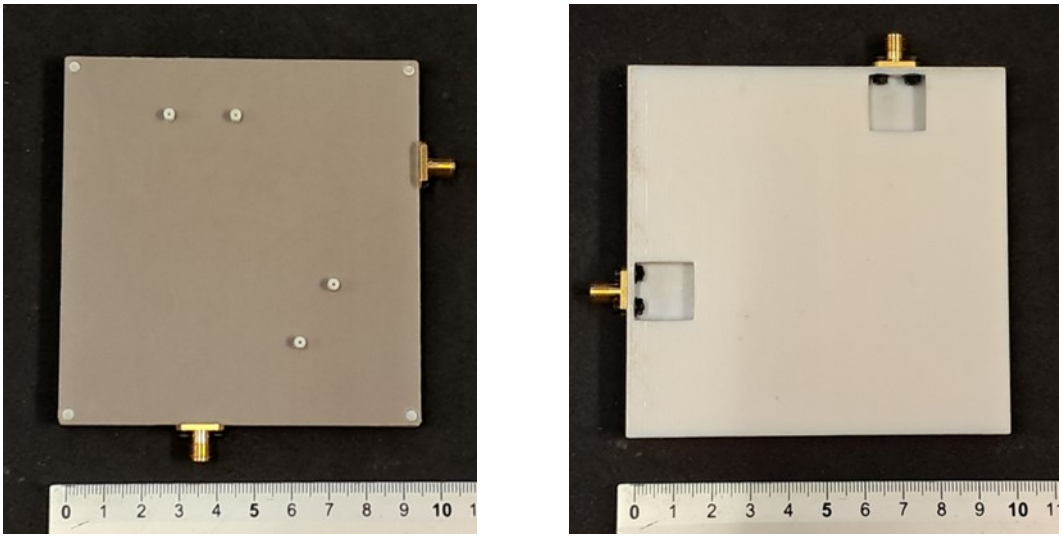

a) *b)*

Figure 3.8 – Assembled prototype: (*a*) top side; (*b*) bottom side with the transitions fixed with screws.

3.2 Measurements

In order to assess the performances of the fabricated prototype, various Liquids Under Test (LUTs) have been injected with a syringe into the containers.

The liquids which have been considered for the validation are isopropanol and acetone, both individually and mixed with different proportions. In this case, since the liquids are real, it is necessary to include losses.

The object of the measurements is the frequency response of the scattering parameter S_{31} between 2 GHz and 3 GHz.

To make measurements, the prototype has been connected to a Vector Network Analyzer (VNA) “Keysight E5080B”, which has been calibrated with the calibration kit “HP 85052D” before taking measurements.

The Figure 3.9 shows the workstation where the measurements have been made.

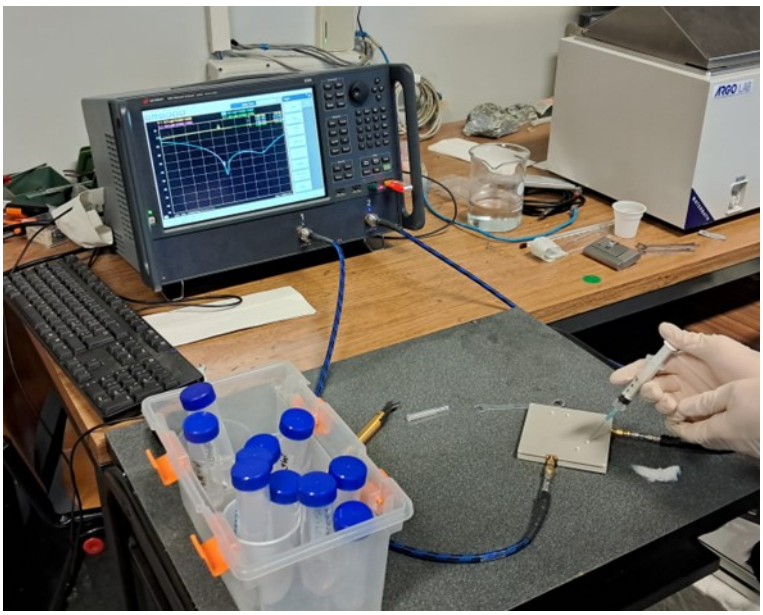

Figure 3.9 – Injection of liquid inside a container while the sensor is connected to the VNA.

The dielectric properties of the LUTs have been obtained using the commercial dielectric probe "Keysight N1501A", which has been calibrated using air, short circuit and water at 21°C. The mixtures used to validate the prototype are listed in Table 3.1, where there are specified the measured values of the real part of the relative dielectric constant, ε_r', and the measured dielectric loss tangent, $\tan\delta = \frac{\varepsilon_r''}{\varepsilon_r'}$, at 2.45 GHz, close to the frequencies of interest.

Mixture	ε_r'	tanδ
Isopropanol	4.37	0.633
80% Isopropanol – 20% Acetone	9.3	0.483
60% Isopropanol – 40% Acetone	14.02	0.292
50% Isopropanol – 50% Acetone	15.85	0.22
40% Isopropanol – 60% Acetone	17.57	0.153
20% Isopropanol – 80% Acetone	19.72	0.075
Acetone	21.62	0.034

Table 3.1 – List of the mixtures used in measurements, each one with the measured real part of the relative dielectric constant and the measured dielectric loss tangent at 2.45 GHz.

The measurements have been structured following these passages:

1) The container holding Sample B is left empty and Sample A changes.
2) The container holding Sample A is left empty and Sample B changes.
3) Sample B is the mixture of 50% isopropanol and 50% acetone, and Sample A changes.
4) Sample A is the mixture of 50% isopropanol and 50% acetone, and Sample B changes.

Specifically, the results coming from the VNA are compared with the simulations made with HFSS, in which the dielectric properties of each mixture have been specified.

3.2.1 Sample B container is empty

In the first part of the measurements, inside the container holding Sample B, it has not been injected anything (so $\varepsilon'_{rB} = 1$) while, in the other one, a mixture - which changes for each step of the analysis - has been injected.

The graphs below represent the frequency response of S_{31}: the continuous line denotes the measured data, while the dashed line the simulated data.

The study starts from the case in which both the containers are air-filled, so the dielectric constants ε_{rB} and ε_{rA} are both equal to 1. Here, as shown in Figure 3.10, the curves exhibit a double resonance peak: these peaks are closer to each other in the measurements' curve with respect to the other one. In particular, the minima are reached at about 2.5 GHz (precisely at 2.462 GHz in the curve of measurements and at 2.515 GHz in the other one), confirming the fact that, when the two samples are the same, the minimum will be reached around the central frequency. The frequency shift between simulations and measurements is due to fabrication tolerances and to an uncertainty in the dielectric properties of the containers.

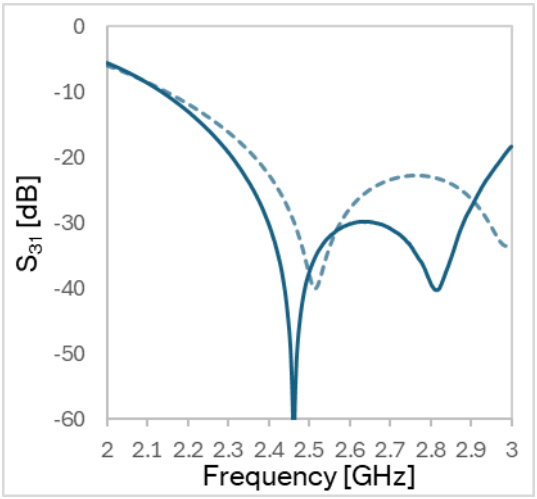

Figure 3.10 – Frequency response when air is in both Sample B and Sample A ($\varepsilon'_{rB} = \varepsilon'_{rA} = 1$). The continuous line represents the measurements, the dashed line the simulation.

In the following step, Sample A is the isopropanol (ε'_{rA} = 4.37; tanδ = 0.633). Looking at the Figure 3.11, the frequency response does not have resonance peaks, and the measurements exhibit a minimum at 2.615 GHz. It can be noticed that the behaviour of the measured values is not particularly different from that of the simulated ones.

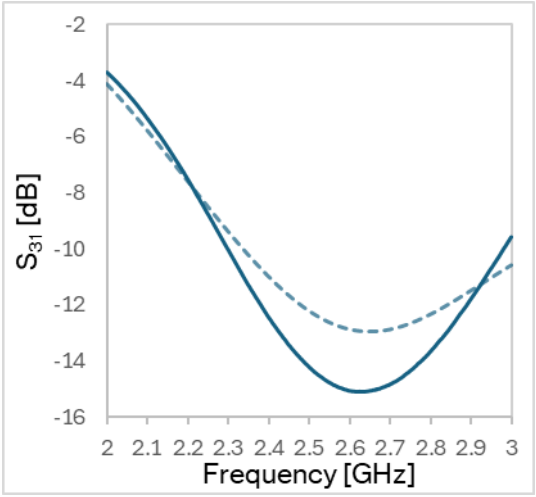

Figure 3.11 – Frequency response when Sample A is isopropanol.
Continuous line: measurements; dashed line: simulation.

Passing to the other liquid mixtures under test, it can be observed, in the following pictures (Figures 3.12 and 3.13), that the performance of the prototype is quite similar to the case of isopropanol. This fact is detectable both in simulations and measurements. In general, it can be noted that the minimum values tend to increase at the rising of the relative permittivity.

To study better this trend, it is possible to analyze the relation between the transmission levels of S_{31}, in correspondence of a specific frequency, and the relative permittivity of the mixtures. In Figure 3.14a, it is reported the trend at 2.462 GHz, the frequency value in which it is measured the minimum when both the containers are air-filled. In Figure 3.14b, it is displayed the behaviour at 2.5 GHz. In both cases, it is possible to remark that the amplitude of S_{31} is extremely

low when Sample A has a relative permittivity equal to that of Sample B, which is 1. When ε'_{rA} grows, the magnitude of S_{31} increases first very rapidly, and then very slowly, assuming at the end an almost flat trend.

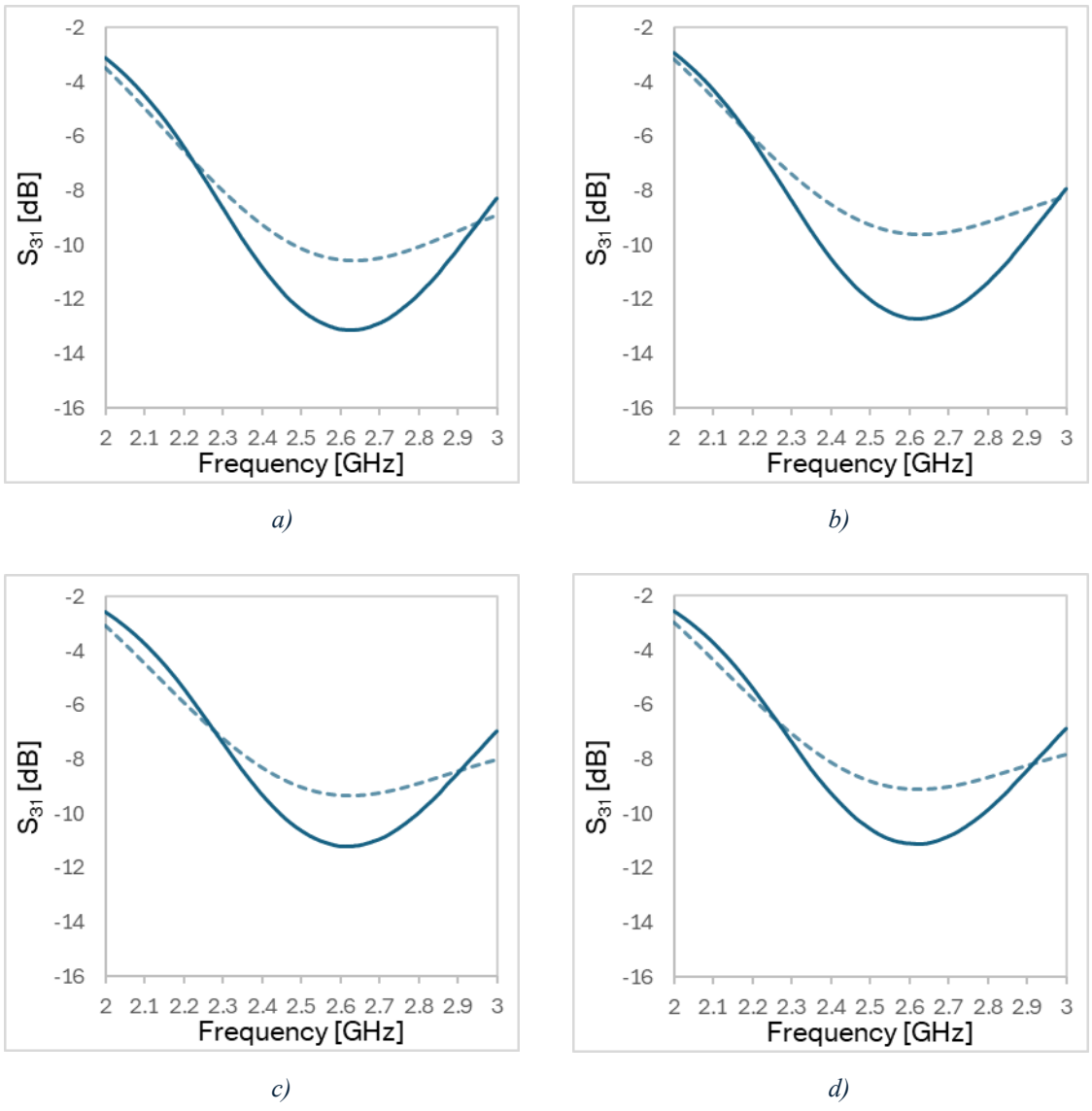

Figure 3.12 – Evolution of the frequency response of S_{31}, for each mixture in Sample A: (*a*) 80% isopropanol and 20% acetone; (*b*) 60% isopropanol and 40% acetone; (*c*) 50% isopropanol and 50% acetone; (*d*) 40% isopropanol and 60% acetone.
Continuous line: measurements; dashed line: simulations.

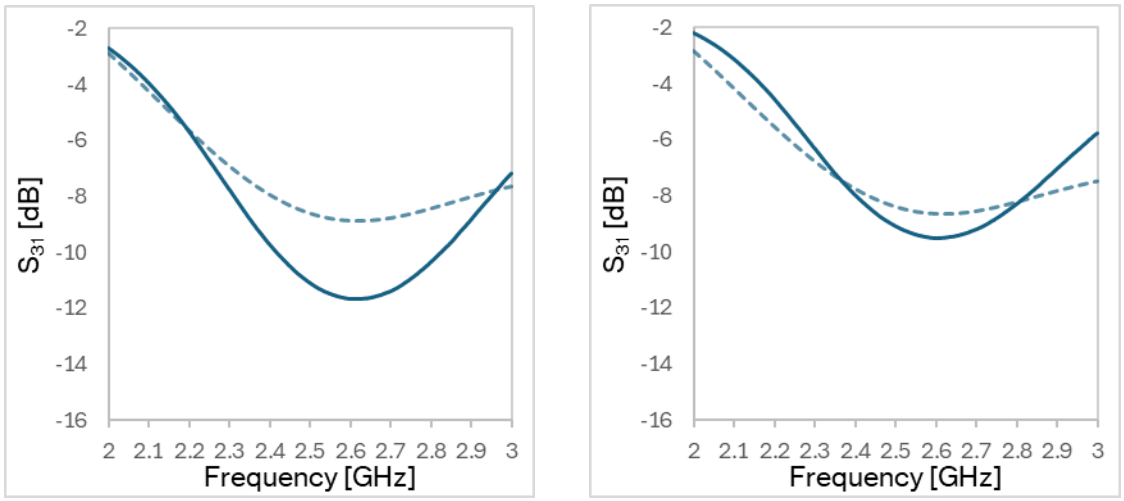

a) *b)*

Figure 3.13 – Evolution of the frequency response of S_{31}, for each mixture in Sample A: (*a*) 20% isopropanol and 80% acetone; (*b*) acetone.
Continuous line: measurements; dashed line: simulations.

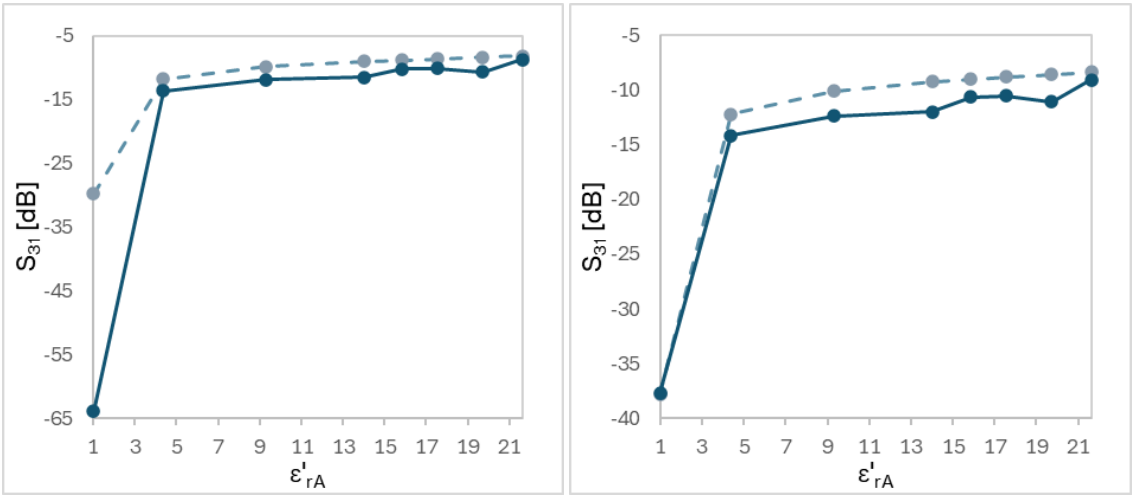

a) *b)*

Figure 3.14 – Magnitude of S_{31} at 2.462 GHz (*a*) and 2.5 GHz (*b*), related to ε'_{rA}.
Comparison between measurements (continuous line) and simulations (dashed line).

3.2.2 Sample A container is empty

The following step of the measurements involves the opposite situation: Sample A is constituted by air ($\varepsilon'_{rA} = 1$), and Sample B is a mixture which changes for each step of the analysis.

To make these measurements, a new container has been inserted in place of the one used to inject the liquids in the previous stage.

Starting from the case in which the two samples are identical (thus $\varepsilon'_{rB} = 1$), the prototype behaves like in the previous phase of measurements: as visible in Figure 3.15a, S_{31} has two negative resonance peaks, with a minimum of amplitude at about 2.5 GHz (at 2.496 GHz to be exact).

At this point, in the container of Sample B, for each step, there have been injected the LUTs for the measurements.

From the isopropanol to the acetone, passing through the mixtures of these two substances, the performances of the prototype assume a similar behaviour (as depicted in the Figures 3.15b, 3.16 and 3.17). Specifically, in the considered band, the double peaks are still present, but they tend to move away from each other: the one on the left tends to get close to the lower limit of the band (2 GHz), while the other one occurs above the upper limit (3 GHz).

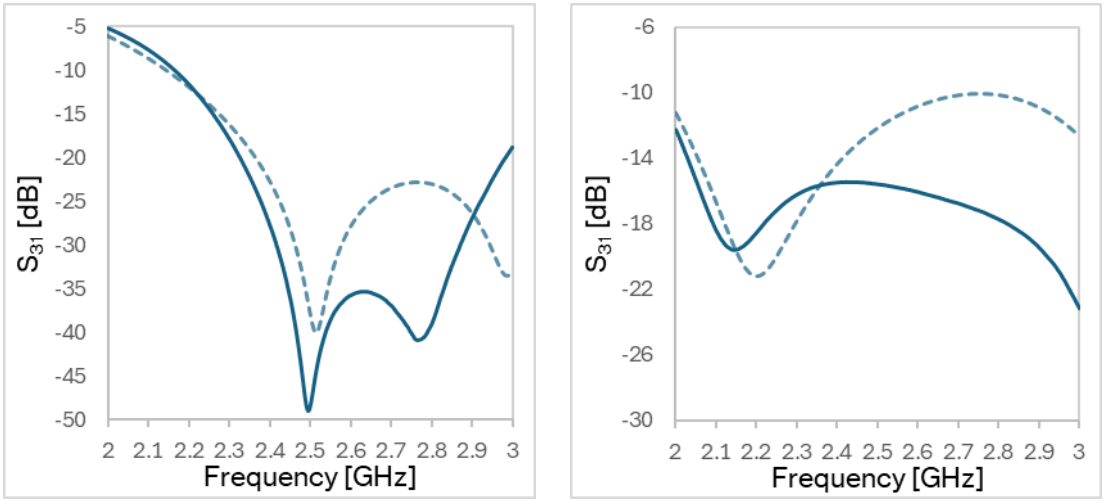

a) *b)*

Figure 3.15 - Evolution of the frequency response of S_{31} for each mixture in Sample B: (*a*) air; (*b*) isopropanol.
Continuous line: measurements; dashed line: simulations.

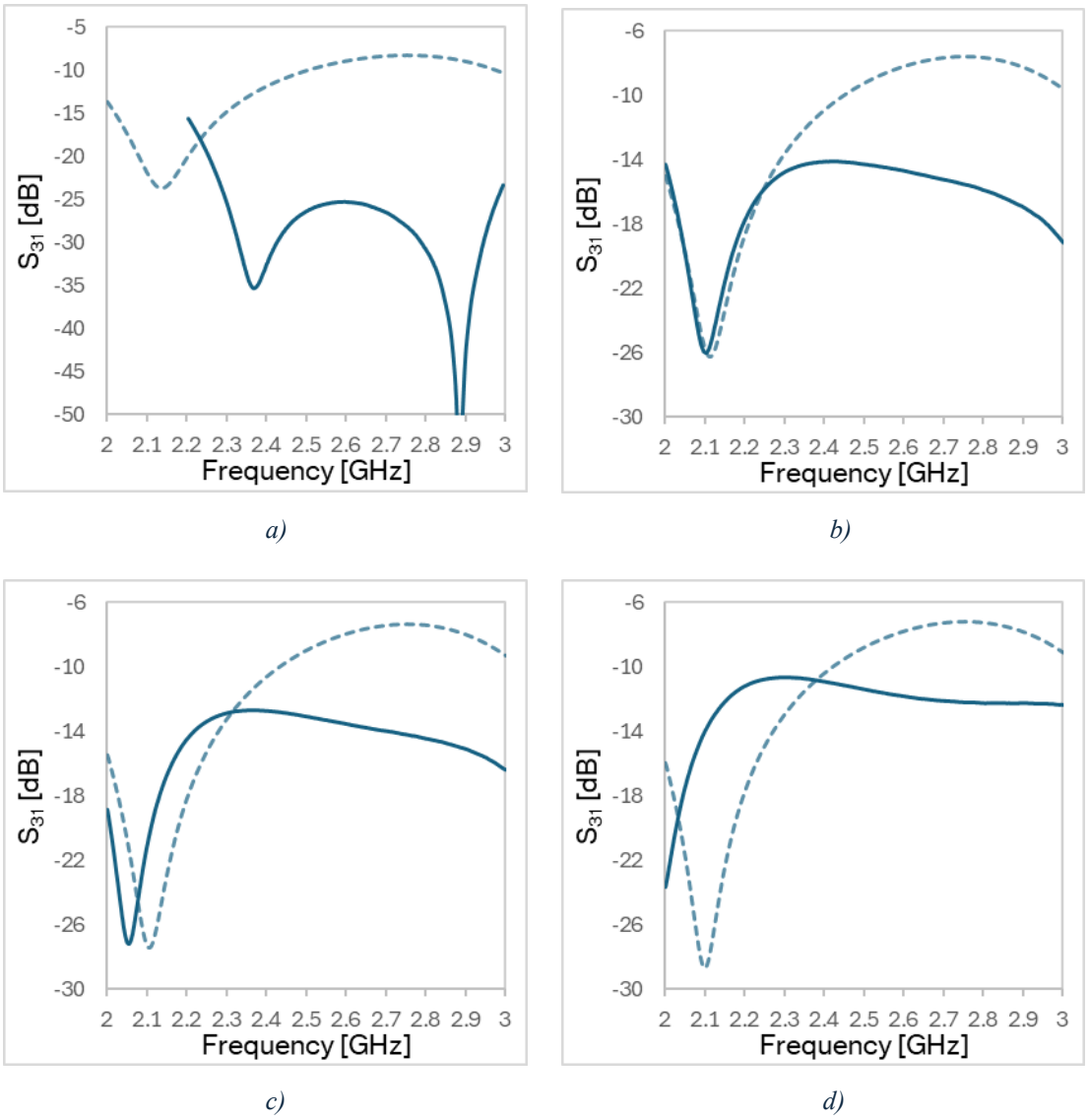

Figure 3.16 - Evolution of the frequency response of S_{31} for each mixture in Sample B: (*a*) 80% isopropanol and 20% acetone; (*b*) 60% isopropanol and 40% acetone; (*c*) 50% isopropanol and 50% acetone; (*d*) 40% isopropanol and 60% acetone.
Continuous line: measurements; dashed line: simulations.

It can be noticed that, in Figure 3.16a, the measurements outcomes are different from the other ones. Here, the double peaks are closer than the other cases, so the curve is more similar to the case in which the Sample B container is empty. In this case, the liquid sample has certainly included an air bubble that - lowering the relative permittivity - has altered the result.

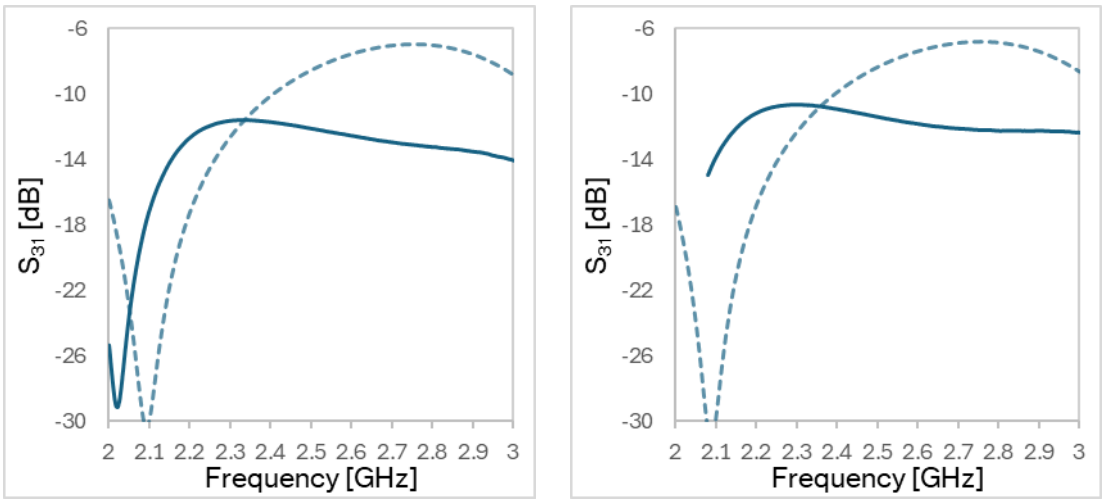

a) *b)*

Figure 3.17 - Evolution of the frequency response of S_{31}, for each mixture in Sample B: (*a*) 20% isopropanol and 80% acetone; (*b*) acetone.
Continuous line: measurements; dashed line: simulations.

In Figure 3.17b, even if some measured data are lost, it can be noted that, for frequencies close to 2 GHz, there is a negative resonant peak.

Finally, in Figure 3.18, it is reported the behaviour of the amplitudes of S_{31} at 2.5 GHz with respect to the relative permittivity. It results not particularly different from that of the previous stage of the study (Fig. 3.14).

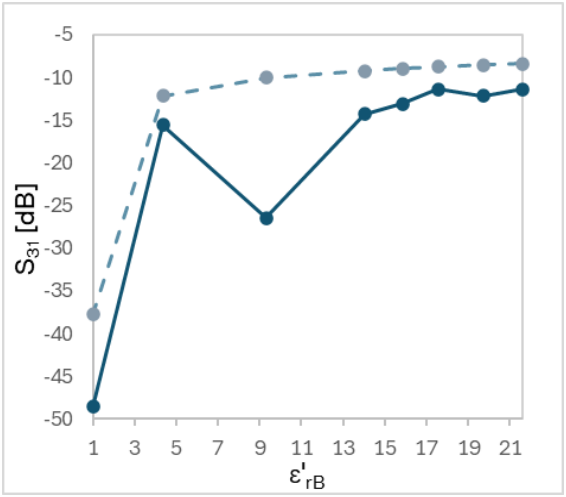

Figure 3.18 - Amplitude of S_{31} at 2.5 GHz, related to ε'_{rB}.
Continuous line: measurements; dashed line: simulations.

3.2.3 Sample B composed of 50% isopropanol and 50% acetone

At this point, the study is focused on a differential analysis of the prototype. Specifically, one of the two samples is fixed, and it is represented by the mixture consisting of 50% isopropanol and 50% acetone, while the other changes.

In the first stage of this part of the analysis, the fixed liquid has been injected in the container of Sample B. Hence, three LUTs have been injected into the other container: 60% isopropanol and 40% acetone; 50% isopropanol and 50% acetone; 40% isopropanol and 60% acetone.

Beginning from the first LUT, as it can be seen in Figure 3.19a, according to the simulations, the frequency response should exhibit two resonance peaks in the considered band. Actually, the measured frequency response does not demonstrate exactly this trend, but the amplitude of S_{31} traces a curve with a minimum at about 2.5 GHz.

Going forward with the other two LUTs, it can be noticed that the results are quite similar to the first one, as reported in Figures 3.19b and 3.19c.

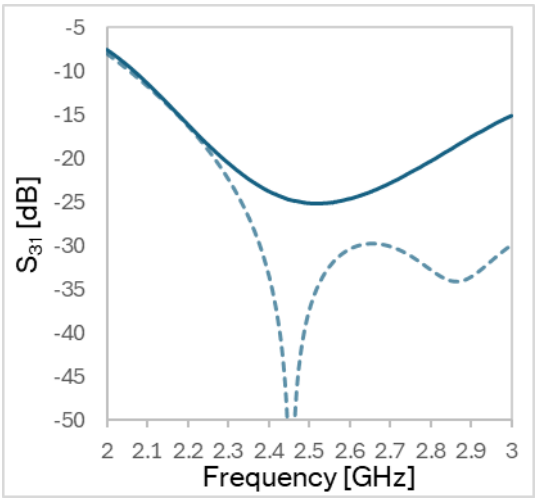

a)

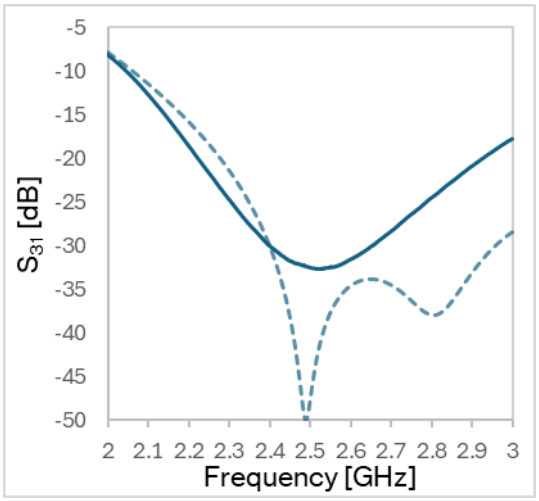

b)

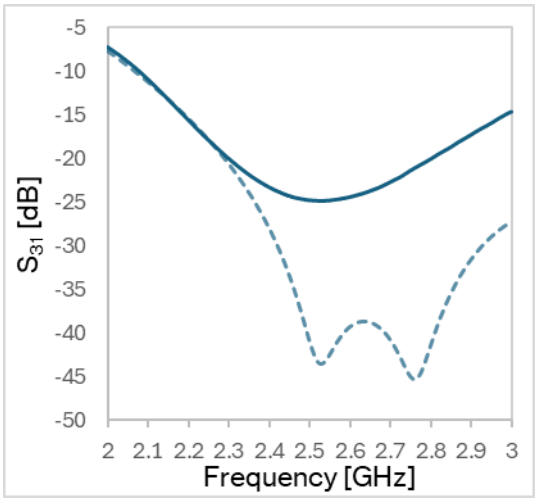

c)

Figure 3.19 - Evolution of the frequency response of S_{31}, for each mixture in Sample A: (*a*) 60% isopropanol and 40% acetone; (b) 50% isopropanol and 50% acetone; (*c*) 40% isopropanol and 60% acetone.

Continuous line: measurements; dashed line: simulations.

In conclusion, in Figure 3.20, the magnitudes of S_{31} at 2.5 GHz are represented in relation to the relative permittivity. The curve shape of the measured data is similar to the curve of simulated data, presenting a minimum when the two samples are equal, as expected in this situation. However, in terms of absolute values, the measured magnitudes appear quite higher than the simulated ones.

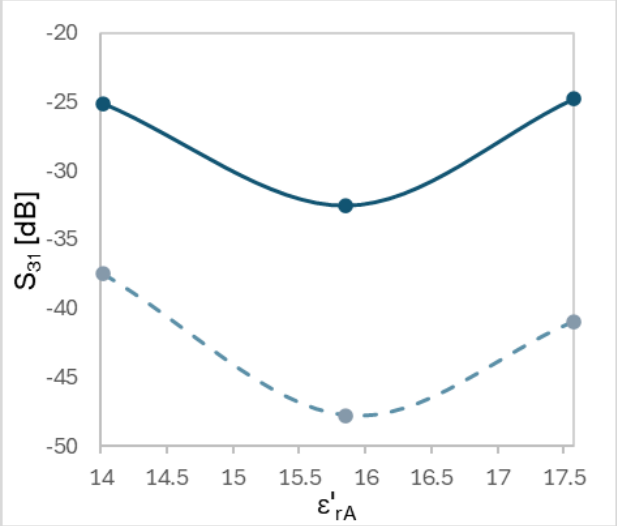

Figure 3.20 - Amplitude of S_{31} at 2.5 GHz related to ε'_{rA}.
Continuous line: measurements; dashed line: simulations.

3.2.4 Sample A composed of 50% isopropanol and 50% acetone

Subsequently, the fixed liquid mixture employed in the previous stage has been injected in the container of Sample A. To make the analysis, there have been used the same three LUTs of the previous case: 60% isopropanol and 40% acetone; 50% isopropanol and 50% acetone; 40% isopropanol and 60% acetone.

Looking at the frequency responses in Figure 3.22, the simulation data report a double resonance peak. This trend is somehow confirmed by measurements, although without a clear distinction between the two peaks.

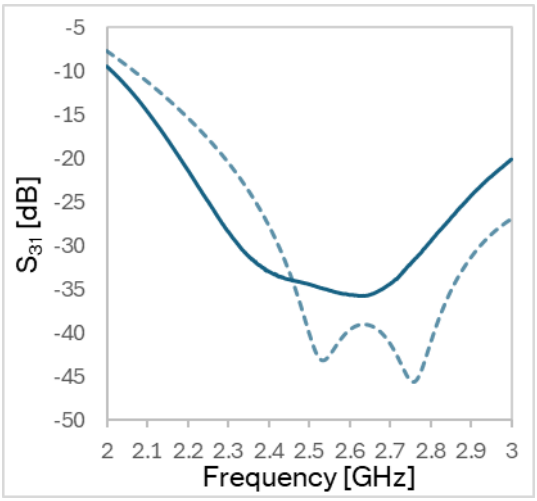

a)

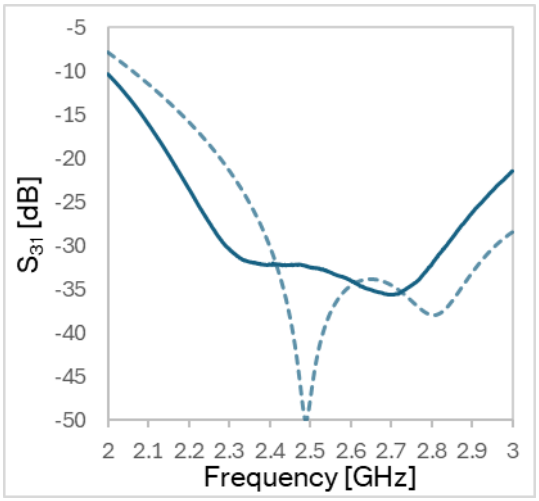

b)

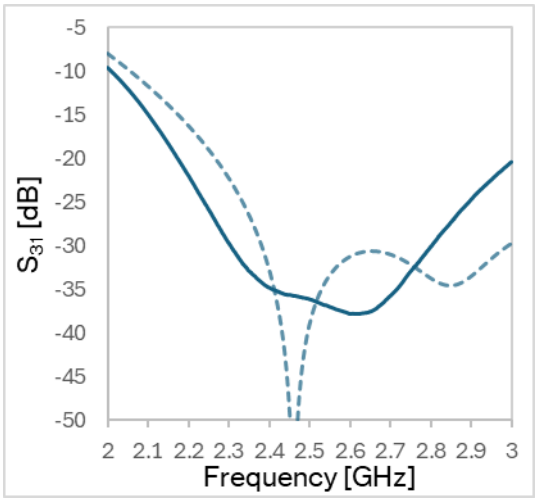

c)

Figure 3.22 - Evolution of the frequency response of S_{31}, for each mixture in Sample B: (*a*) 60% isopropanol and 40% acetone; (*b*) 50% isopropanol and 50% acetone; (*c*) 40% isopropanol and 60% acetone.

Continuous line: measurements; dashed line: simulations.

The consequence is observable in the graph reporting the amplitudes of S_{31} at 2.5 GHz in relation to the relative permittivity (Figure 3.23). Here, measurements reveal a different performance with respect to the simulation data. In fact, instead of having a minimum in correspondence of the situation in which the two samples are equal, the curve shows a maximum in that point.

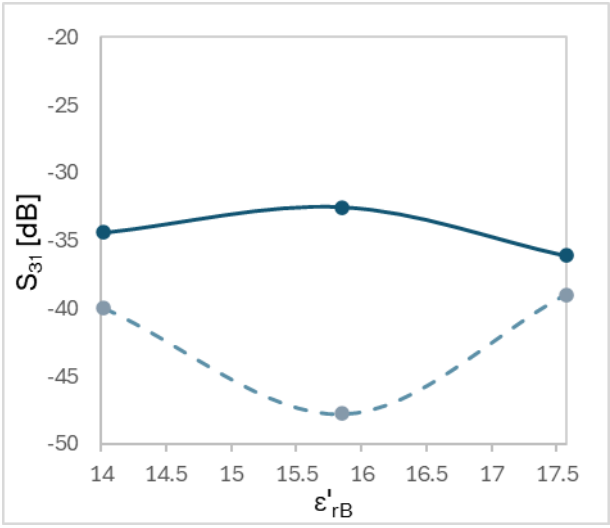

Figure 3.23 - Amplitude of S_{31} at 2.5 GHz, related to ε'_{rB}.
Continuous line: measurements; dashed line: simulations.

3.3 Model function of the sensor

At the end, the purpose is to create a model in which, from a measured value of S_{31}, it is possible to predict the relative dielectric constant ε_r of the LUT.

Referring to the situations in which air is the reference sample (Paragraphs 3.2.1 and 3.2.2), the simulation data have been taken in order to obtain a function to find ε_r. A relation able to describe the simulated behaviour of the sensor - with a reduced amount of error - can be the following one:

$$\varepsilon_r = ae^{bx} + 1,$$

where $a = 1535.1$ and $b = 0.5139$.

Because the sensor delivers raw data to user, it is necessary to calibrate the detected values, in order to reduce the error rate. To make it, two known materials are taken as reference for the calibration: air and acetone. Firstly, simulated and measured data are scaled, making the difference between the parameters S_{31} when the LUTs are acetone and air, both for simulations and measurements, as follows:

$$scale_{simulation} = Simulation_{acetone} - Simulation_{air}$$

$$scale_{measure} = Measure_{acetone} - Measure_{air}$$

Then, the value of S_{31} detected by the sensor ($Measure$) is multiplied by the ratio between $scale_{simulation}$ and $scale_{measure}$. This quantity must be reduced by an offset, corresponding to the difference between the value of S_{31} detected by the sensor when the material is air ($Measure_{air}$) multiplied by $\frac{scale_{simulation}}{scale_{measure}}$ and the simulation value of S_{31} when the material is air ($Simulation_{air}$). The result obtained corresponds to the calibrated value of S_{31} detected by the sensor ($Measure_{calibrated}$). This calculation is summarized below:

$$Measure_{calibrated} = (Measure - Measure_{air})\frac{scale_{simulation}}{scale_{measure}} + Simulation_{air}$$

At the end, with the calibrated value of S_{31} detected by sensor, it is possible to determine the correspondent value of the relative permittivity, using in this way the function exposed before:

$$\varepsilon_r = ae^{b*(Measure_{calibrated})} + 1$$

The results have been plotted for each LUT, in the graphs in Figure 3.24, where each value of ε_r detected by the sensor is compared to the relative permittivity sensed by the commercial probe. The outcome is not particularly accurate, but it can be noticed in Figure 3.24b that, when the LUT is composed of 80% isopropanol and 20% acetone, the resulting ε_r is close to 1, confirming the presence of air in the container during the measurement.

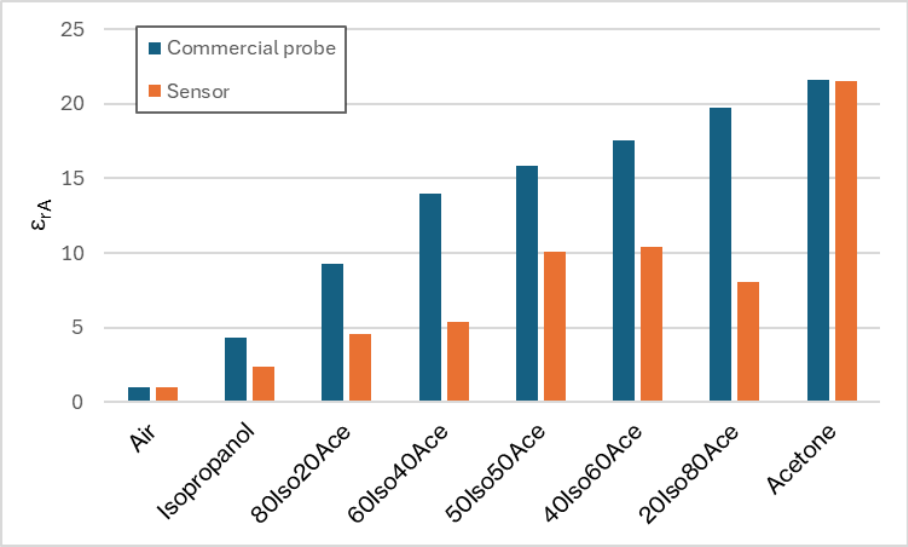

a)

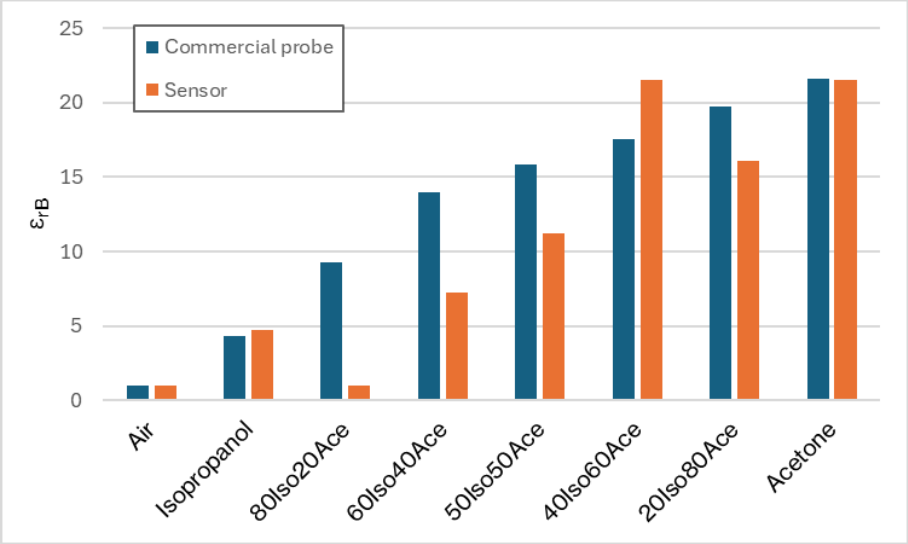

b)

Fig 3.24 – Values of ε_r for each LUT detected by the sensor (orange) and compared to the values sensed by the commercial probe (blue). (*a*) Sample B is air; (*b*) Sample A is air.

Conclusions

Dielectric sensors are devices which can characterize accurately materials in a not expensive way, with the possibility to employ small components. They exploit the interaction of an electromagnetic field on a dielectric material. Several studies have proposed topologies of these sensors.

In this work, the purpose is to design and realize a differential dielectric sensor for liquid materials characterization. It is based on a rat-race coupler, made using the inverted microstrip technology, combined with two containers holding different liquid materials. The dielectric characteristics of a liquid can be derived by comparing the reflection properties of this fluid with a known calibration material.

Initially, as illustrated in Chapter 2, the proposed topology has been founded on a rectangular rat-race: because the resulting structure appears unbalanced, this hypothesis has been later rejected in favour of a symmetrical circular rat-race configuration. To give the right dimensioning to the sensor, the structure has been analysed using the simulation tool Ansys HFSS. In these simulations, there have been used lossless materials with arbitrary relative dielectric constants.

Once obtained the right dimensions, as shown in Chapter 3, a prototype has been fabricated, using a hybrid technology, combining the standard printed circuit board (PCB), to build the inverted microstrip, with 3D printing, to fabricate the containers and the support structure. To validate the prototype, different liquids have been employed. There have been considered isopropanol and acetone, both in absolute form and mixed, with different proportions. Hence, the prototype has been measured, and its behaviour has been compared with simulations.

Using the prototype, there has been found an issue, related to the container, which can be improved to obtain a more accurate sensor. In particular, when the liquid has to be extracted after measurements, some drops remain trapped inside. Hence, before to make further measurements, it is necessary to wait until the remaining

liquid evaporates. In this way, a real-time analysis is prevented. This drawback could be overcome changing the shape of the containers, or their dimensions. Moreover, they could be manufactured with other technologies, for example glass tubes.

This work has been realized with the collaboration of the Microwave Laboratory of the University of Pavia.

References

[1] L. F. Chen, C. K. Ong, C. P. Neo, V. V. Varadan, V. K. Varadan, “Microwave Electronics: Measurement and Materials Characterization”, John Wiley & Sons, 2004.

[2] F. Jafari and M. Rad Malekshahi, "A Low-Cost Microwave Microfluidic Sensor Based on Planar Ring Resonator," in *IEEE Sensors Journal*, vol. 23, no. 18, pp. 21070-21077, 15 Sept.15, 2023.

[3] K. S. L. Parvathi and S. R. Gupta, "Ultrahigh-Sensitivity and Compact EBG-Based Microwave Sensor for Liquid Characterization," in IEEE Sensors Letters, vol. 6, no. 4, pp. 1-4, April 2022.

[4] G. M. Rocco, M. Bozzi, D. Schreurs, L. Perregrini, S. Marconi, G. Alaimo, F. Auricchio, "3-D Printed Microfluidic Sensor in SIW Technology for Liquids’ Characterization," in IEEE Transactions on Microwave Theory and Techniques, vol. 68, no. 3, pp. 1175-1184, March 2020.

[5] T. Chretiennot, D. Dubuc and K. Grenier, "A Microwave and Microfluidic Planar Resonator for Efficient and Accurate Complex Permittivity Characterization of Aqueous Solutions," in IEEE Transactions on Microwave Theory and Techniques, vol. 61, no. 2, pp. 972-978, Feb. 2013.

[6] S. Rustioni, L. Silvestri, S. Marconi, G. Alaimo, F. Auricchio and M. Bozzi, "A Dielectric Permittivity Sensor Based on Inverted Microstrip/3D-Printing Hybrid Technology," 2024 IEEE/MTT-S International Microwave Symposium - IMS 2024, Washington, DC, USA, 2024, pp. 883-886.

[7] A. Ebrahimi, G. Beziuk and K. Ghorbani, "Amplitude Variation Microwave Sensors for High-Sensitivity Detection of Solid and Microfluidic Dielectrics," in *IEEE Transactions on Microwave Theory and Techniques*, vol. 72, no. 11, pp. 6460-6472, Nov. 2024.

[8] A. Ebrahimi and K. Ghorbani, "High-Sensitivity Detection of Solid and Liquid Dielectrics Using a Branch Line Coupler Sensor," in *IEEE Transactions on Microwave Theory and Techniques*, vol. 71, no. 12, pp. 5233-5245, Dec. 2023.

[9] I. Piekarz, J. Sorocki, N. Delmonte, L. Silvestri, S. Marconi, G. Alaimo, F. Auricchio, M. Bozzi, "Microwave-Microfluidic Sensor in Hybrid 3-D Printing and Laminate Technology for Chemicals Monitoring from Differential Reflection," 2021 IEEE MTT-S International Microwave Symposium (IMS), Atlanta, GA, USA, 2021.

[10] X. Han, K. Liu and S. Zhang, "High-Sensitivity Dual-Band Microfluidic Microwave Sensor for Liquid Dielectric Characterization," in *IEEE Sensors Journal*, vol. 24, no. 22, pp. 36689-36697, 15 Nov.15, 2024.

[11] B. Allain, N. Delmonte, L. Silvestri, S. Marconi, G. Alaimo, F. Auricchio, M. Bozzi, "Exploiting the Coupling Variation of 3-D-Printed Cavity Filters for Complex Dielectric Permittivity Sensing," in IEEE Microwave and Wireless Technology Letters, vol. 34, no. 6, pp. 717-720, June 2024.

[12] M. A. Masoumabad, N. Delmonte, L. Silvestri, L. Perregrini and M. Bozzi, "A Simple Technique for Liquid–Liquid Percentage Determination Using Single-Frequency Amplitude Measurements," in *IEEE Microwave and Wireless Technology Letters*, vol. 33, no. 7, pp. 1086-1089, July 2023.

[13] A. K. Jha, N. Delmonte, A. Lamecki, M. Mrozowski and M. Bozzi, "Design of Microwave-Based Angular Displacement Sensor," in IEEE Microwave and Wireless Components Letters, vol. 29, no. 4, pp. 306-308, April 2019.

[14] M. V. Schneider, "Microstrip lines for microwave integrated circuits," in The Bell System Technical Journal, vol. 48, no. 5, pp. 1421-1444, May-June 1969.

[15] D.M. Pozar, “Microwave Engineering”, 4th Edition, John Wiley & Sons, 2012.

[16] J. Sorocki, I. Piekarz, N. Delmonte, L. Silvestri and M. Bozzi, "A Broadband Inline Transition from On-PCB Microstrip to Hybrid Stack-Up Integrated Additively Fabricated Air-Filled Waveguide," in IEEE Access, vol. 12, pp. 7884-7895, 2024.

[17] I. Piekarz, J. Sorocki, N. Delmonte, L. Silvestri, S. Marconi, G. Alaimo, F. Auricchio, M. Bozzi, "Wideband Microstrip to 3-D-Printed Air-Filled Waveguide Transition Using a Radiation Probe," in IEEE Microwave and Wireless Components Letters, vol. 32, no. 10, pp. 1179-1182, Oct. 2022.

[18] J. Sorocki, I. Piekarz, A. Samulak, N. Delmonte, L. Silvestri, S. Marconi, G. Alaimo, F. Auricchio, M. Bozzi, "Additively Fabricated Air-Filled Waveguide Integrated with Printed Circuit Board Using a Through-Patch Transition," in IEEE Microwave and Wireless Components Letters, vol. 31, no. 11, pp. 1207-1210, Nov. 2021.

[19] H. García-Martínez, G. Torregrosa-Penalva, E. Àvila-Navarro, N. Delmonte, L. Silvestri and M. Bozzi, "3D-Printed Electromagnetic Band-Gap Band-Pass Filter Based on Empty Single-Ridge Waveguide," in IEEE Access, vol. 10, pp. 53954-53962, 2022.

[20] H. García-Martínez, E. Avila-Navarro, G. Torregrosa-Penalva, N. Delmonte, L. Silvestri, S. Marconi, G. Alaimo, F. Auricchio, M. Bozzi, "Design and Fabrication of a Band-Pass Filter with EBG Single-Ridge Waveguide Using Additive Manufacturing Techniques," in IEEE Transactions on Microwave Theory and Techniques, vol. 68, no. 10, pp. 4361-4368, Oct. 2020.